



Attributing and Verifying European and National Greenhouse Gas and Aerosol Emissions and Reconciliation with Statistical Bottom-up Estimates

Deliverable 2.5

Report on European N₂O inversions

Authors:	Joël Thanwerdas (Empa) Arjo Segers (TNO) Sophie van Mil (TNO) Dominik Brunner (Empa)
Date:	2025-12-04
Dissemination:	Public
Work package:	2.5
Version:	1



**Funded by
the European Union**

This project has received funding from the European Union's Horizon Europe research and innovation programme under grant agreement No. 101081322

Views and opinions expressed are however those of the author(s) only and do not necessarily reflect those of the European Union or the Climate, Infrastructure and Environment Executive Agency (CINEA). Neither the European Union nor the granting authority can be held responsible for them.

Attributing and Verifying European and National Greenhouse Gas and Aerosol Emissions and Reconciliation with Statistical Bottom-up Estimates (AVENGERS)

Call: HORIZON-CL5-2022-D1-02

Topic: HORIZON-CL5-2022-D1-02-01

Type of action: HORIZON Research and Innovation Actions

Granting authority: European Climate, Infrastructure and Environment Executive Agency

Project starting date: 01/01/2023

Project end date: 30/06/2026

Project duration: 42 months

Contact: Dr. Marko Scholze, Coordinator
Lund University, Sweden

Document history:

Version	Author(s)	Date	Changes
1	All	2025-12-04	Initial version

Internal review: ULUND

Contents

1	Executive summary	4
2	Introduction	4
2.1	Background	4
2.2	Scope of this deliverable	5
2.2.1	Objectives of this deliverable	5
2.2.2	Work performed in this deliverable	5
2.2.3	Deviations and counter measures	5
3	Input data	6
3.1	Prior fluxes	6
3.2	Background concentrations	7
3.3	Atmospheric observations	7
4	Description of inversion systems	9
4.1	CIF-ICON-ART	9
4.1.1	Transport model	9
4.1.2	Inversion system and algorithm	9
4.1.3	State vector	10
4.1.4	Prior and observation errors	10
4.2	LOTOS-EUROS	12
4.2.1	Transport model	12
4.2.2	Model updates	13
4.2.3	Inversion system and algorithm	14
4.2.4	Observation representation error	17
4.2.5	Background correction	19
4.3	Comparison of setups	20
5	Results	22
5.1	Prior and posterior mole fractions	22
5.2	Flux adjustments	25
5.3	Analysis of posterior fluxes	28
6	Discussion and conclusion	33

1 Executive summary

2 Introduction

2.1 Background

Nitrous oxide (N₂O) is a potent greenhouse gas (GHG) and the third most significant anthropogenic contributor to global warming after carbon dioxide (CO₂) and methane (CH₄). Although its atmospheric concentration is much lower than that of CO₂ or CH₄, N₂O has a global warming potential approximately 273 times greater than CO₂ over a 100-year timescale (Forster et al., 2021). Moreover, N₂O is now the dominant ozone-depleting substance emitted in the 21st century, following the decline of chlorofluorocarbons (CFCs) (World Meteorological Organization, 2022). Its dual impact, both as a greenhouse gas and as a substance that destroys stratospheric ozone, makes it a critical target for climate and environmental policy.

The global atmospheric concentration of N₂O has been increasing steadily since the pre-industrial era, rising from about 270 parts per billion (ppb) in 1750 to 337 ppb today (Lan et al., 2022). This growth is mainly driven by human activities, particularly those related to agriculture. Microbial processes such as nitrification and denitrification in soils release N₂O as a by-product of nitrogen cycling. The use of synthetic nitrogen fertilizers, manure application, and the cultivation of nitrogen-fixing crops enhance these microbial activities, making agricultural soils the dominant anthropogenic source of N₂O worldwide (Tian et al., 2024). Other sources include fossil fuel combustion, biomass burning, wastewater treatment, and certain industrial processes such as nitric and adipic acid production (Tian et al., 2024).

Quantifying N₂O emissions remains a major challenge due to their strong spatial heterogeneity and pronounced seasonal variability, driven by factors such as temperature, soil moisture, and agricultural practices. Emission estimates can be derived through two main methodological frameworks: bottom-up and top-down approaches. The bottom-up approach relies on emission factors combined with activity data to infer emissions from individual sources. While this method provides detailed sectoral insights, it is often resource-intensive, time-consuming, and typically subject to reporting delays of up to two years. In contrast, the top-down approach (also referred to as inverse modeling) integrates atmospheric transport models with statistical data assimilation techniques. By incorporating observed atmospheric GHG concentrations, often within Bayesian frameworks, this method refines prior (bottom-up) emission inventories to produce posterior estimates that are consistent with atmospheric observations. As acknowledged in the 2019 Refinement to the 2006 IPCC Guidelines for National Greenhouse Gas Inventories (Calvo Buendia et al., 2019), top-down methods serve as a valuable complement to bottom-up inventories, helping to reconcile discrepancies and improve overall emission assessments. However, the accuracy of these top-down estimates depends critically on the spatial coverage, temporal resolution, and precision of available atmospheric measurements.

To enhance the measurement of atmospheric GHG concentrations and surface–atmosphere–ocean fluxes, the European Union established the Integrated Carbon Observation System (ICOS; Heiskanen et al., 2022). ICOS is a world-class, standardized, and open-access observational network comprising approximately 180 stations across 16 European countries, encompassing three station types:

atmospheric, ecosystem, and oceanic. Since its inception in the early 2010s, ICOS has steadily expanded its observational capacity. As of today, the atmospheric network includes 28 stations conducting continuous N₂O measurements, compared with only 14 stations in 2010. This expanded observational coverage, together with improvements in measurement precision, provides a stronger foundation for constraining European N₂O emissions. Ultimately, such enhanced estimates can support the development of more effective climate mitigation policies and contribute to the long-term protection of both the climate system and the ozone layer.

In Task 2.5 of the EU-HORIZON project AVENGERS, we performed atmospheric inversions of European N₂O emissions over the period 2010-2023 using two different inversion systems. The results are presented in this deliverable.

2.2 Scope of this deliverable

2.2.1 Objectives of this deliverable

The objective of this deliverable is to present the European N₂O inversions conducted within the AVENGERS project using two distinct inversion systems. This report provides detailed descriptions of the inversion systems, the input datasets, and the resulting analyses obtained from this exercise.

2.2.2 Work performed in this deliverable

In addition to the European N₂O inversions, specific technical developments were undertaken to couple the transport model ICON-ART with the Community Inversion Framework (CIF) for this deliverable. Furthermore, several enhancements and corrections were implemented to improve the performance and robustness of LOTOS-EUROS system.

2.2.3 Deviations and counter measures

The Vrije Universiteit Amsterdam (VU), which operates the CTDAS-WRF inversion system, was unable to deliver the N₂O European inversions in time, as their efforts were focused on CH₄. As a result, the conclusions of this work rely on only two inversion systems, limiting the robustness of the findings.

TNO, operating LOTOS-EUROS, could not provide posterior uncertainties in time. Consequently, the posterior uncertainties reported in this study are based solely on a single inversion system: CIF-ICON-ART.

These delayed results will be released at a later date, and the data will be made available on the ICOS Carbon Portal.

3 Input data

3.1 Prior fluxes

Anthropogenic N₂O fluxes are derived from the TNO-AVENGERS (TNO-GHGco_v7) inventory (Dröge et al., 2024). The approach to prepare the TNO-AVENGERS inventory is similar to CAMS-REG.v4 (Kuenen et al., 2022), but now also includes N₂O emissions of all sectors and CO₂, CH₄ and N₂O emissions from the LULUCF sector. Country totals are based on UNFCCC national inventory reports, while emissions are spatially distributed using sector-specific proxies at a horizontal resolution of 0.05° × 0.1° across Europe. The dataset also provides temporal scaling factors (hour-of-day, day-of-week, and month-of-year), enabling the construction of hourly emission fields from the spatially distributed data.

In addition, the inventory includes estimates of indirect N₂O emissions from agricultural sources via leaching and runoff, following Wang et al. (2023), and from non-agricultural sources through atmospheric nitrogen deposition. For the latter, EMEP (European Monitoring and Evaluation Programme) produced a 0.1° × 0.1° gridded dataset of deposited oxidized nitrogen (OXN) and reduced nitrogen (RDN) over Europe for 2010–2022 to complement TNO data. It is assumed that RDN originates from agricultural activities and is therefore already included in the main country reporting provided by TNO. To avoid double counting, we thus only consider OXN, which is treated as entirely non-agricultural. TNO converted the OXN deposition data to N₂O emissions using an emission factor of 0.010 kg N₂O–N (kg N)⁻¹ (1%). This additional dataset is provided as an add-on to the first TNO-AVENGERS release.

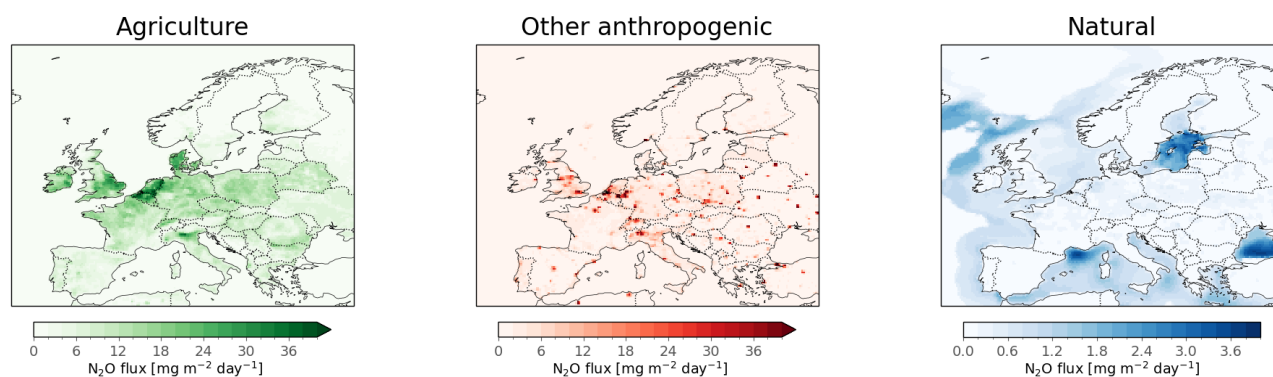


Figure 1: Spatial distributions of prior emissions from agricultural, other anthropogenic, and natural source categories, averaged over 2010–2023. Note that the color scale for natural emissions differs from that used for the agricultural and other anthropogenic categories.

We also account for natural N₂O emissions from inland freshwaters (rivers, lakes, and reservoirs) and continental shelves. For inland waters, we use the gridded estimates from Li et al. (2024), which provide N₂O emissions for 1850–2019. The 1850–1880 mean is used to represent natural (pre-industrial) fluxes. For continental shelves, we apply a multi-model estimate of global N₂O emissions at 0.5° × 0.5° resolution (Resplandy et al., 2024). This climatological dataset represents

the mean of four models, and, consistent with methodology applied in the global N₂O budget (Tian et al., 2024), these emissions are assumed to be entirely natural.

All emission maps are displayed in Figure 1.

3.2 Background concentrations

Initial conditions and lateral boundary conditions for N₂O mole fractions are derived from the Copernicus Atmospheric Monitoring Service (CAMS) global inversion-optimized N₂O concentration product v22r1 (Chevallier and Thompson, 2024). The product is obtained by assimilating surface observations only and is provided at a horizontal resolution of $2.50^\circ \times 1.27^\circ$ (longitude by latitude) and at a 3-hourly temporal resolution.

3.3 Atmospheric observations

We assimilate observations from the dataset "Collection of historic and ongoing N₂O observations across Europe (release 2024-11)" (Henne et al., 2024). This dataset integrates both historical and contemporary N₂O measurements from multiple European networks and individual institutions. Within the temporal and spatial domains of our experiments, data are available from 33 continuous monitoring stations (see Fig. 2) and from flask samples collected at 10 stations in the NOAA network. Detailed information on all stations is provided in Table 1 and in Karstens (2023).

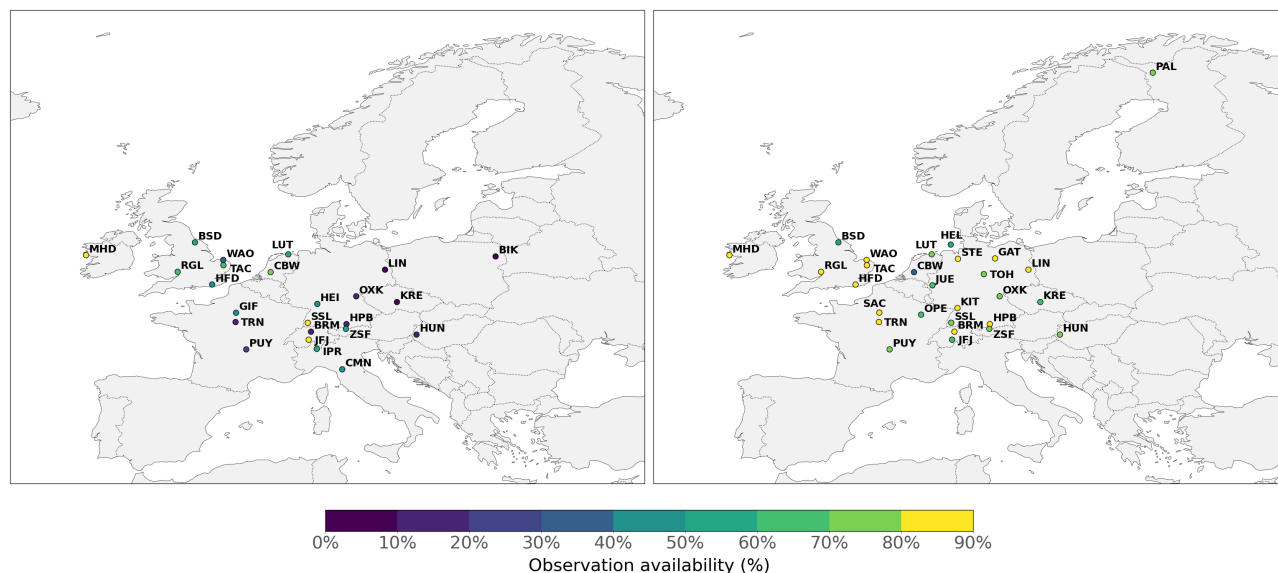


Figure 2: Locations of stations conducting continuous N₂O measurements. The color shading within each circle denotes data availability, expressed as the percentage of valid hourly observations for 2010–2018 (left panel) and 2019–2023 (right panel).

Table 1: List of stations monitoring N₂O mole fractions across Europe and basic associated metadata, such as geographic location, altitude of the stations (ground level, in meter above sea level), height of the sampling inlet (in meter above ground level) and type of data (C for continuous in situ measurements and F for flask). For tall towers, only measurements at the highest levels of the stations will be assimilated, therefore only these measurements are listed here. Time-averaged values used to prescribe the model–data mismatch (observation error) are shown for each station. MDM.C corresponds to the model–data mismatch (in ppb) derived from CIF-ICON-ART, and MDM.L corresponds to the mismatch derived from LOTOS-EUROS.

Code	Type	Fullname	Country	Latitude	Longitude	Altitude	Intake height	MDM.C	MDM.L
BIK	C	Białystok	POL	53.23	23.01	183	300	0.70	1.12
BRM	C	Beromünster	CHE	47.19	8.18	797	212	0.45	0.29
BSD	C	Bilsdale	GBR	54.36	-1.15	382	248	0.34	0.34
CBW	C	Cabauw	NLD	51.97	4.93	0	207	0.68	0.44
CMN	C	Monte Cimone	ITA	44.17	10.68	2165	7	0.70	2.38
GAT	C	Gartow	DEU	53.07	11.44	69	341	0.43	0.33
GIF	C	Gif sur Yvette	FRA	48.71	2.15	160	7	0.55	0.41
HEI	C	Heidelberg	DEU	49.42	8.68	113	30	0.63	0.34
HEL	C	Helgoland	DEU	54.18	7.88	43	110	0.54	0.43
HFD	C	Heathfield	GBR	50.98	0.23	207	100	0.49	0.46
HPB	C	Hohenpeissenberg	DEU	47.80	11.02	934	131	0.39	0.36
HUN	C	Hegyhatsal	HUN	46.95	16.63	248	82	0.59	0.69
IPR	C	Ispra	ITA	45.81	8.64	210	16	0.72	0.60
IZO	C	Izaña	ESP	28.31	-16.50	2373	29		
JFJ	C	Jungfraujoch	CHE	46.55	7.99	3580	10	0.39	0.47
JUE	C	Jülich	DEU	50.91	6.41	98	120	0.47	0.25
KIT	C	Karlsruhe	DEU	49.09	8.42	110	200	0.45	0.50
KRE	C	Křešín u Pacova	CZE	49.57	15.08	534	250	0.44	0.37
LIN	C	Lindenberg	DEU	52.17	14.12	73	98	0.40	0.31
LUT	C	Lutjewad	NLD	53.40	6.35	1	60	1.14	0.97
MHD	C	Mace Head	IRL	53.33	-9.90	8	3	0.30	0.28
OPE	C	Observatoire pérenne de l'environnement	FRA	48.56	5.50	390	120	0.38	0.35
OXK	C	Ochsenkopf	DEU	50.03	11.81	1022	163	0.48	0.62
PAL	C	Pallas	FIN	67.97	24.12	560	12	0.30	0.24
PUY	C	Puy de Dôme	FRA	45.77	2.97	1465	10	0.45	0.41
RGL	C	Ridge Hill	GBR	52.00	-2.54	207	90	0.41	0.34
SAC	C	Sa clay	FRA	48.72	2.14	160	100	0.42	0.33
SSL	C	Schauinsland	DEU	47.90	7.92	1205	6	0.53	0.50
STE	C	Steinkimmen	DEU	53.04	8.46	29	252	0.51	0.43
TAC	C	Tacolneston	GBR	52.52	1.14	64	100	0.40	0.28
TOH	C	Torfhaus	DEU	51.81	10.54	801	147	0.40	0.35
TRN	C	Trainou	FRA	47.96	2.11	131	180	0.49	0.37
WAO	C	Weybourne Atmospheric Observatory	GBR	52.95	1.12	31	10	0.60	0.40
ZSF	C	Zugspitze-Schneefernerhaus	DEU	47.42	10.98	2656	3	0.32	0.25
BAL	F	Baltic Sea	POL	55.35	17.21	3	25	0.52	0.26
BSC	F	Black Sea, Constanta	ROU	44.18	28.66	0	5		
CIB	F	Centro de Investigacion de la Baja Atmosfera (CIBA)	ESP	41.81	-4.93	845	2	0.38	0.27
HPB	F	Hohenpeissenberg	DEU	47.80	11.02	985	5	0.44	0.28
HUN	F	Hegyhatsal	HUN	46.96	16.65	248	96	0.49	0.40
LMP	F	Lampedusa	ITA	35.52	12.62	45	5	0.54	0.29
MHD	F	Mace Head	IRL	53.32	-9.90	5	21	0.36	0.29
OXK	F	Ochsenkopf	DEU	50.03	11.81	1022	150	0.43	0.22
PAL	F	Pallas	FIN	67.97	24.12	565	5	0.32	0.30
TAC	F	Tacolneston	GBR	52.52	1.14	56	180	0.44	0.26

4 Description of inversion systems

4.1 CIF-ICON-ART

4.1.1 Transport model

The Icosahedral Nonhydrostatic (ICON) weather and climate model (Zängl et al., 2015) is a collaborative effort between the Deutscher Wetterdienst (DWD), the Max Planck Institute for Meteorology (MPI-M), the Deutsches Klimarechenzentrum (DKRZ), the Karlsruhe Institute of Technology (KIT), and the Center for Climate Systems Modeling (C2SM) in Switzerland. Its goal is to develop a unified, next-generation global system for numerical weather prediction (NWP) and climate modeling. ICON became operational within DWD's and MeteoSwiss' forecasting systems in 2015 and 2024, respectively. Notably, ICON was made available as open-source software to expand its user and developer community in February 2024. To incorporate atmospheric chemistry and aerosol processes, ICON is extended by the Aerosols and Reactive Trace gases (ART) module, developed and maintained by KIT (Hoshyaripour et al., 2025; Schröter et al., 2018; Rieger et al., 2015). This combination forms the ICON-ART model, a non-hydrostatic Eulerian chemical transport model that includes emissions, transport, gas-phase chemistry, and aerosol dynamics in both the troposphere and stratosphere. ICON-ART uses an icosahedral grid that can cover the entire globe or be restricted to limited areas, ranging in horizontal resolution from several degrees down to a few kilometers.

For the present study, the model is configured with a horizontal resolution of 26 km (approximately 0.3°) over Europe (15°E – 35°E, 33° N – 73° N), consisting of 21,344 grid cells. Vertically, the model extends from the surface up to 23 km with 60 levels, using a height-based, terrain-following coordinate system. Meteorological variables are computed online by the ICON model. Key prognostic variables (including wind speed, specific humidity, density, virtual potential temperature, and Exner pressure), are weakly nudged toward ERA5 reanalysis data (Hersbach et al., 2023, 2017) from the ECMWF, available at a 3-hourly temporal resolution. This nudging helps maintain the model's realism and prevents significant drift from observed atmospheric conditions. ERA5 data also provide the model's initial state. Emission fields for transported species are processed via the Online Emissions Module (OEM; Jähn et al., 2020), integrated within ART. Output files of instantaneous concentrations are saved hourly and later interpolated in time, height, and space to derive model equivalents of observational data.

4.1.2 Inversion system and algorithm

Inversions are performed with the Community Inversion Framework (CIF; Berchet et al., 2021). CIF is a system that has been designed to bring together the different inversion methods (analytical, variational and ensemble) and transport models used in the inversion community. It is built as an open-source, well documented, highly modular multi-model inversion framework written in Python that facilitates the comparison of (1) inversion methods and (2) transport models. CIF has proved to be accurate and computationally performant over the past years (Wittig et al., 2023; Savas et al., 2023; Remaud et al., 2022; Thanwerdas et al., 2024, 2022b,a)

We employ the ensemble square root filter (EnSRF) algorithm implemented in CIF to perform

the inversions presented in this study. This algorithm has recently been improved and is thoroughly described in Thanwerdas et al. (2025). Briefly, an ensemble of vectors is used to represent the probability distribution of the state vector (also called control vector), which contains all the variables that we wish to optimize (e.g., fluxes, background concentrations, etc). Each member of the ensemble is attached to a different tracer transported by the model. After running simulations with this ensemble of tracers, the resulting ensemble of output concentrations is used to optimize the state vector to minimize the mismatch with the assimilated observations of atmospheric concentrations.

4.1.3 State vector

In this study, we independently optimize three categories of N₂O emissions: agricultural emissions (ANTH-AGRI), other anthropogenic non-agricultural emissions (ANTH-OTHERS), and natural emissions (NAT). The anthropogenic emissions are separated into agricultural and non-agricultural components for two main reasons: (1) agricultural emissions dominate the overall anthropogenic N₂O budget, and (2) their spatial distribution is more diffuse compared to the more localized non-agricultural sources, which are primarily associated with industrial activities. In addition, we optimize both the background N₂O concentrations (defining the initial atmospheric state at the start of the simulation), and the boundary inflow conditions (representing N₂O transported into the regional domain from external regions).

Emission fluxes are optimized at the level of individual grid cells across the horizontal domain. Background concentrations are optimized across 32 inflow regions. They are defined as radial sectors, each covering an equal angular region centered on the midpoint of the domain's latitude–longitude extent (see Fig. 3). Initial concentrations are optimized using the full extent of the 32 regions, whereas boundary concentrations throughout the simulation are optimized along the domain borders only. As the CAMS global inversion-optimized N₂O concentration product v22r1 does not provide concentrations for 2023, the values in 2022 were extended using an offset of 1.02 ppb (Lan et al., 2025).

The full assimilation period is partitioned into consecutive 10-day windows. Within each window, a single scaling factor is assigned to every optimized variable. The scaling factors are optimized using observations from both the current window and the subsequent window (i.e., the number of lags is set to 2). To suppress spurious long-range correlations within the ensemble, covariance localization is applied using an exponential decay function with a characteristic decay length of 600 km, following the recommendations of Thanwerdas et al. (2025).

To reduce the total runtime, each year is inverted independently, preceded by a one-month spin-up and followed by a one-month spin-down.

4.1.4 Prior and observation errors

Uncertainties in both the prior information and the observations are represented through covariance matrices, which quantify the assumed statistical relationships between optimized variables. The prior-error covariance matrix characterizes uncertainties in the a priori flux estimates, while the observation-error covariance matrix accounts for uncertainties in the assimilated measurements

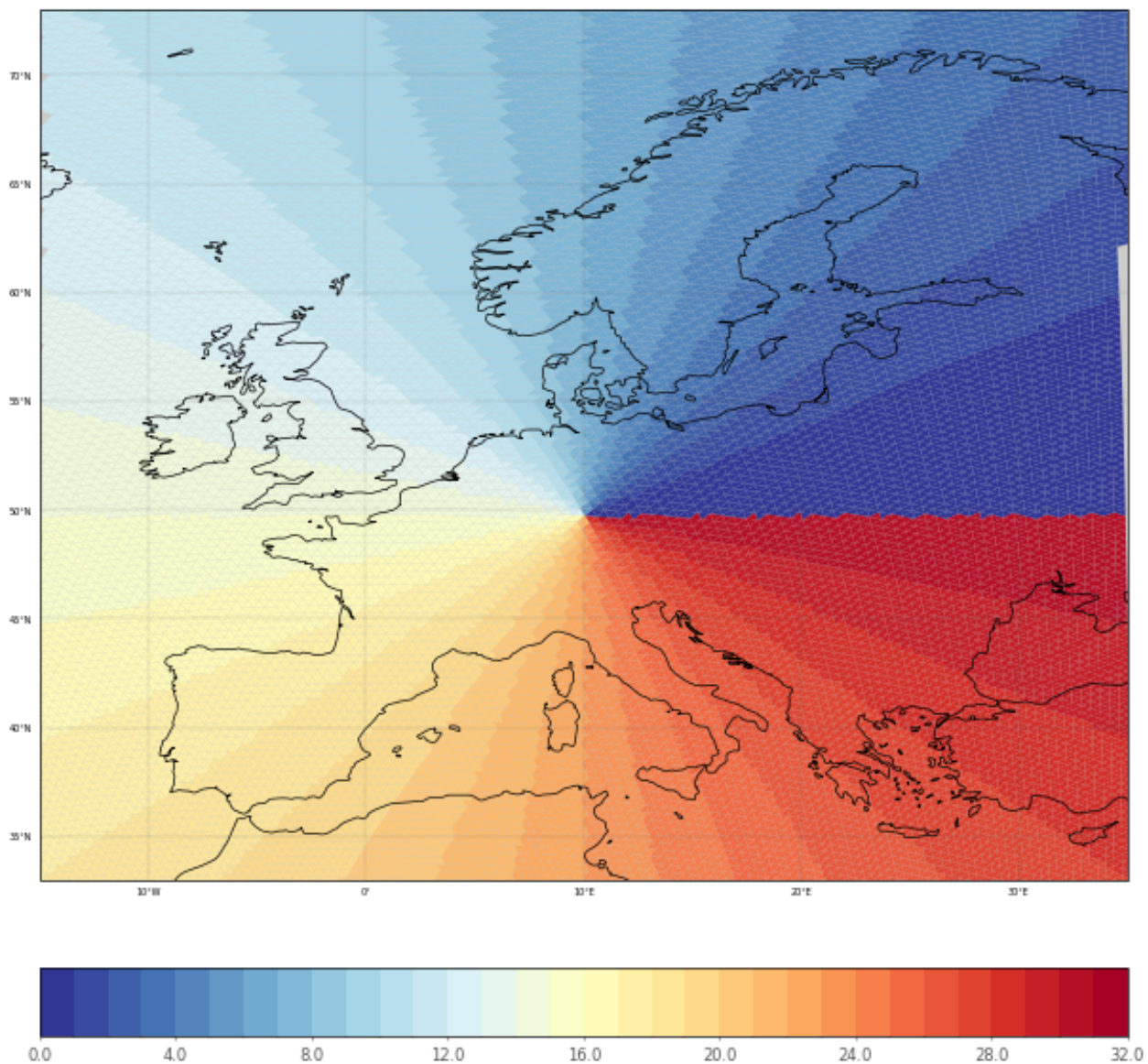


Figure 3: Definition of the 32 inflow regions used to optimize background concentrations in CIF-ICON-ART. The entire regions are used to optimize initial concentrations only. The boundary concentrations are optimized using these regions along the domain borders.

and in the modeled atmospheric transport. All errors are assumed to follow a normal (Gaussian) probability distribution.

For the scaling factors associated with surface fluxes, we prescribe a relative standard deviation of 100% (square-root of diagonal elements of the covariance matrix). Spatial correlations are represented through a correlation matrix constructed using an exponential decay function, $e^{-\frac{d_{i,j}}{L}}$, where $d_{i,j}$ denotes the great-circle distance between cells i and j , and L is the spatial correlation length. These correlations are then multiplied by the corresponding variances to form the off-diagonal elements of the covariance matrix.

The spatial correlation length was estimated by TNO (included in the TNO-AVENGERS dataset) to be approximately 70 km for ANTH-AGRI and 50 km for ANTH-OTHERS (Dröge et al., 2024). In contrast, several recent studies have adopted considerably larger values, typically in the range of 200–500 km (e.g., Tian et al., 2024; Petrescu et al., 2023; Thompson et al., 2014).

Szénási et al. (2021) estimated correlation lengths of 100–150 km for agricultural (ANTH-AGRI) methane emissions, while assuming negligible spatial correlation for non-agricultural (ANTH-OTHERS) sources. These findings suggest that realistic correlation lengths for anthropogenic emissions are relatively short, generally below 100 km. However, adopting such small values in our inversion framework would substantially limit the number of effective observational constraints, given the sparse spatial coverage of assimilated measurements. Moreover, for consistency and comparability with previous studies, we adopt intermediate correlation lengths, defined as follows:

- 150 km for ANTH-AGRI,
- 100 km for ANTH-OTHERS, and
- 200 km for NAT.

For the scaling factors associated with background concentrations, we use a relative variance of 0.5% (~ 1.5 ppb) and a large-scale correlation length of approximately 2000 km, following the value estimated by Szénási et al. (2021) for methane. The parameters are summarized in Table 2.

The observation error is computed based on a series of forward and inverse simulations. We first perform a forward simulation for all the years. Simulated values are then sampled and compared to observations to compute an initial estimate of observation error using the root mean square error (RMSE). This estimate is used to perform a first inversion for the period 2010-2023. Following the inversion, we recalculate the RMSE, which serves as a refined estimate of the observation error for these stations.

4.2 LOTOS-EUROS

4.2.1 Transport model

The LOTOS-EUROS model (Manders et al., 2017) is a regional chemistry transport model (CTM) driven by offline meteorological data. The main application is in full chemistry simulations including trace gases and aerosols related to air quality and deposition, but the model could also be configured

Table 2: Comparison of elements of state vector and parameters of prior-error covariance matrix. σ denotes the relative prior uncertainty (standard deviation of the probability distribution). L and τ are the spatial and temporal correlation lengths, respectively.

		EMISSION CATEGORY			BACKGROUND
		ANTH-AGRI	ANTH-OTHERS	NATURAL	
Probability distribution of prior errors	CIF-ICON-ART	Normal	Normal	Normal	Normal
	LOTOS-EUROS	Semi-exponential	Semi-exponential	Semi-exponential	Normal
σ	CIF-ICON-ART	100%	100%	100%	1.5 ppb
	LOTOS-EUROS	100%	100%	100%	0.3 ppb
L	CIF-ICON-ART	150 km	100 km	200 km	2000 km
	LOTOS-EUROS	100 km	100 km	100 km	1200 km
τ	CIF-ICON-ART	3 months	3 months	3 months	3 months
	LOTOS-EUROS	1 month	1 month	1 month	3 months

to simulate concentrations of greenhouse gases. Simulation of N₂O mixing ratios in LOTOS-EUROS has been newly developed for this study.

Following the protocol defined for the N₂O inversions, the model domain covers Europe (15° E – 35° E, 33° N – 73° N). Horizontally, the model was configured to use a regular longitude-latitude grid of 0.50° × 0.25° (approximately 25 km in the middle of the domain). In the vertical, 21 hybrid sigma-pressure layers are used with the first layer approximately 20 m thick and a top at 200 hPa (tropopause). These layers are a coarsening of the 137 model layers used in the ECMWF ERA5 reanalysis (Hersbach et al., 2020), from which the meteorological data was taken. The use of reanalysis data ensured consistent meteorological input for the LOTOS-EUROS simulations during the entire 2010-2013 period of this study.

4.2.2 Model updates

For the purpose of this project, the model has been extended with a N₂O tracer. This is initially filled from the background (section 3.2) and increased by local emissions (section 3.1), and to which then all transport processes in the model are applied (3D advection and vertical mixing). The main sink of N₂O is a photolysis reaction in the stratosphere: as the model covers the troposphere only, this sink is not directly implemented but implicitly represented by inflow of N₂O-poor air at the top boundary.

Initial tests with the N₂O version of the model showed that accurate representation of the vertical transport and the mixing with global background is very important for correct simulation of mixing ratio's at the surface, where the comparison with observations is made. The model has therefore received specific updates for this project:

- The air masses in the model are now defined as dry air rather than humid air as was used before. This ensures correct uptake of the CAMS global background mixing ratio's which are

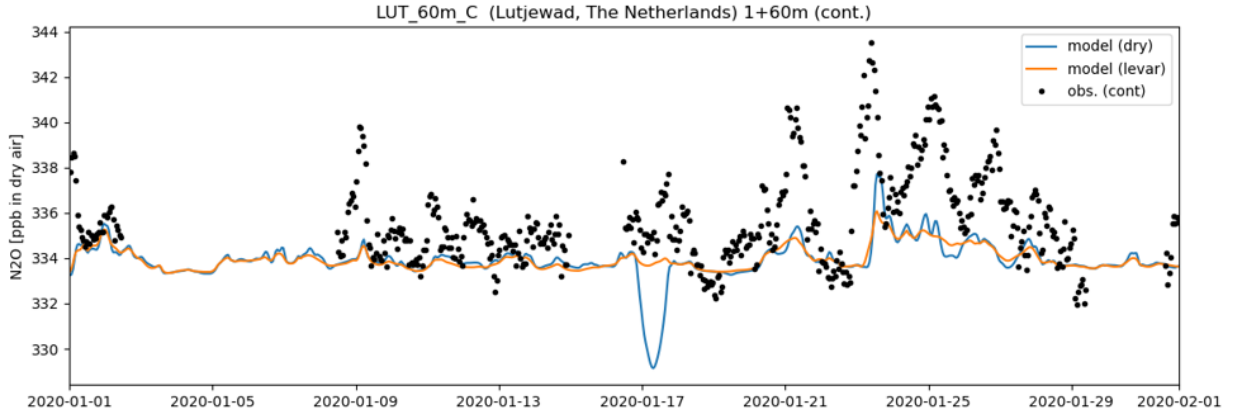


Figure 4: Example of timeseries simulations by LOTOS-EUROS model. The blue line originates from an earlier model simulation, the orange originates from the version with updates dedicated to N₂O simulation.

expressed as dry-air-volume-mixing-ratio's, but also correct simulation of surface observations which are expressed in these units too.

- The number of vertical layers was increased from 12, which is the default when simulating air quality related concentrations, to 21, which is the maximum number available in the extract of ERA5 meteorological data currently available for LOTOS-EUROS.
- The computation of vertical gradients in tracer mixing ratios at the top of the model has been improved for a smoother connection with the global background fields.

The result of the updates is shown in Figure 4. The original model (blue line) occasionally produced sudden low mixing ratio's due to too large inflow of N₂O-poor air from the model top, but these are not present anymore after the updates.

For use in inversion systems, the model could read time series of 2D parameter fields to perturb the model data, for example the emission fields. In addition, the model could run in adjoint mode to compute the sensitivity of observation simulations towards changes in these parameter fields.

4.2.3 Inversion system and algorithm

The emission inversion system around the LOTOS-model is based on the *four-dimensional variational* (4D-VAR) approach, in a framework also used in for example Bergamaschi et al. (2022). In a variational approach, a state vector \mathbf{x} is defined with the parameters to be optimized, for example time series of correction factors applied to the emissions. The optimal \mathbf{x} is defined to be the state for which the following cost function reaches a minimum:

$$J(\mathbf{x}) = 1/2 (\mathbf{x} - \mathbf{x}^b)^T \mathbf{B}^{-1} (\mathbf{x} - \mathbf{x}^b) + 1/2 (H(\mathbf{x}) - \mathbf{y})^T \mathbf{R}^{-1} (H(\mathbf{x}) - \mathbf{y}) \quad (1)$$

The elements of the cost-function define the result of the minimization procedure, and are in this study defined as follows.

- The state vector \mathbf{x} consists of monthly time series of 2D fields, defined on the same regular grid as the model. In total 4 series of fields are defined: one for each of the three main emission sectors, and one for correction of the global background fields (see also table 2 for an overview). The *emission deviation factors* x_s for an emission sector s are used to adjust the emissions in the model using a *semi-exponential* following:

$$\tilde{E}_s(i, t) = \begin{cases} E_c[i, t] (1 + x_s[i, t]) & , x_s \geq 0 \\ E_c[i, t] \exp(x_s[i, t]) & , x_s < 0 \end{cases} \quad (2)$$

where $\tilde{E}_s[i, t]$ denotes the actual emissions by sector s in grid cell i in month t , and $E_c[i, t]$ denotes the corresponding prior emission.

The *background* correction field δc in the state are added to the modeled N₂O mixing ratios before simulations at observation locations are sampled.

- The prior or state \mathbf{x}_b contains the initial values of the state, which is here zero for all elements (neither emission deviation nor background correction).
- The prior covariance matrix \mathbf{B} defines the uncertainty of the state \mathbf{x} . Thus, this defines the freedom that is available to change emissions and background mixing ratios in order to reach the best possible match with observations. Table 2 summarizes the most important parameters of the implementation of the covariance.

For each of the 4 timeseries, the standard deviations are the same per grid cell. For the emission deviation factors they are set to 100%. Actual emissions could therefore be easily 2-3 times as large as the prior, but due to the semi-exponential expansion in Eq. (2) they cannot become negative. For the background correction a standard deviation of 0.3 ppb is assumed, as will be described in more detail in section 4.2.5.

The uncertainties between emissions sectors and also between emissions and background are assumed to be uncorrelated. The remaining correlations per timeseries of fields are separated in a spatial (horizontal) and a temporal part. For the horizontal correlations between cells i and j a Gaussian decay with distance is assumed:

$$\rho(x[i, t], x[j, t]) = \exp(-1/2 |d_{i,j}|^2/L^2) \quad (3)$$

where $d(\cdot)$ denotes the distance between the cells, and L denotes a spatial correlation length scale. For the emission deviation factors a rather small length scale of 100 km is assumed, as emissions could differ strongly regionally based on weather conditions and for example agricultural practices. For the background correction a much longer length scale is assumed, as will be described in section 4.2.5.

For the temporal correlation between two months t_1 and t_2 , an exponential decay is assumed:

$$\rho(x[i, j, t_1], x[i, j, t_2]) = \exp(-|t_2 - t_1|/\tau) \quad (4)$$

where τ is a temporal correlation time scale. For the emission deviations a rather short time scale of 1 month is assumed, as the majority of the emitting process depend on season and

meteorological conditions; for the temporal time scale of the background we refer to section 4.2.5.

- The observations available within an inversion period are collected in y . In this study, the observations consist of ground observations from the ICOS network, as described in section 3.3, and are expressed in ppb volume mixing ratio's in dry air.
- The observation operator $H(\mathbf{x})$ provides a model simulation given the state \mathbf{x} . The operator represents the expansion of the emission deviation factors in the state to actual emissions, transport of emitted tracers by the LOTOS-EUROS model, and sampling of the simulated mixing ratios at the location of the observations. The sampling is done in the grid cell that encloses the location of the ICOS observation site, and at the altitude (above sea level) of the site plus the observation height. The altitude is used rather than just the observation height to ensure that for elevated sites the sample is taken from a higher model layer, as the model surface is probably smoother than the real orography. The background correction δc from the state is added to the simulation. As the model version simulates mixing ratios in dry air, no unit conversions are needed.
- The observation representation error covariance \mathbf{R} describes the stochastic distribution of the difference between the observations and the simulations, in case the later is derived using the (unknown) true state \mathbf{x}^t . This difference is assumed to be a sample of a multivariate normal distribution with zero mean and covariance \mathbf{R} :

$$H(\mathbf{x}^t) - \mathbf{y} \sim \mathcal{N}(\mathbf{o}, \mathbf{R}) \quad (5)$$

Differences between observations and simulations arise from for example:

- instrumental errors, that for many sites are provided with the observation data;
- grid-sampling errors, as the model simulates average mixing ratios in grid boxes while observations are point observations.

In this study we assume that the observation errors are uncorrelated between the observations, thus \mathbf{R} is diagonal. A suitable value for the remaining uncertainty is obtained by tuning, as will be described in section 4.2.4.

With the state and covariances defined and observations collected, the minimum of the cost function in Eq. (1) is searched using an iterative procedure. Each iteration requires one simulation with the standard (forward) LOTOS-EUROS model, and one with the adjoint (backward) model. Evaluation of the forward and adjoint model is the most expensive part of the 4D-Var procedure; if 20 iterations are needed to reach a suitable minimum of the cost function, then 40 simulations are needed. Although in theory possible, it would take too much run time to apply the 4D-Var cycle to the full 2010-2023 period at once. Therefore, the procedure is applied for each year independently, and these inversions could therefore run in parallel next to each other. As the temporal correlations are assumed to be short, the error of optimizing the emissions per year is expected to be small.

However, in future it might be better to define at least a spin-up and spin-down period for each year of 1 or months, to check whether this assumption is actually valid.

As final illustration of the method, Figure 5 shows examples of posterior 2D fields in the state for a single month (April 2019). In this example, the strongest changes are applied to the agricultural emissions, while the other anthropogenic and especially the natural emissions are changed much less. The background corrections are defined to consist of large smooth patterns only, and this is indeed what is visible in the optimized field.

4.2.4 Observation representation error

As described earlier, the observation representation error covariance \mathbf{R} is assumed to be a diagonal matrix (uncorrelated errors). The diagonal elements should be filled with a squared standard deviation for each of the observations in the (yearly) inversion window that are selected for assimilation. In this study, the squared standard deviations are defined as the sum of contributions from an *instrumental* error and the *remaining* error:

$$r_k^2 = r_{instr,k}^2 + r_{remaining,k}^2 \quad (6)$$

where k denotes the index of the observation.

The *instrumental* error standard deviation is set to the value reported in the observation data files, if defined. If this value is not provided, it is set to 0.2 ppb which is the median of the values that are present.

The *remaining* error should account for, for example, the grid cell or time sampling errors. As these are difficult to define, a first estimate is obtained by tuning a value based on observation-minus-simulation statistics. In theory, if the background error covariance \mathbf{B} and the observation representation error covariance \mathbf{R} correctly describe the actual error distributions, then:

$$\mathbf{y} - H(\mathbf{x}^b) \sim \mathcal{N}(\mathbf{0}, \mathbf{H}^T \mathbf{B} \mathbf{H} + \mathbf{R}(\alpha)) \quad (7)$$

where \mathbf{H} is a linearization of $H(\mathbf{x})$ around \mathbf{x}^b , and α represent the parameters of \mathbf{R} to be tuned. With a maximum-likelihood estimation (Henne et al., 2016), the parameters α could be chosen such that the observation-minus-simulation samples are a likely sample out of the distribution. It is usually not possible to evaluate the covariance because the full matrix \mathbf{B} is too large anyhow, and only available in parameterized form. One option is to draw an ensemble of random samples from \mathbf{B} , but this is left for future studies. Instead, if both $\mathbf{H}^T \mathbf{B} \mathbf{H}$ and \mathbf{R} are diagonal, then Eq. (7) could be rewritten to a requirement for individual observations k :

$$\frac{y_k - (H(\mathbf{x}^b))_k}{\sqrt{(\mathbf{H}^T \mathbf{B} \mathbf{H})_{kk} + (\mathbf{R}(\alpha))_{kk}}} \sim \mathcal{N}(0, 1) \quad (8)$$

Here a simple approach is used to represent the diagonal elements of $\mathbf{H}^T \mathbf{B} \mathbf{H}$ using the output of a standard model run, which provides also the N₂O mixing ratio's due to the the global background only. The difference between a full simulation and the background part is a simplified representation of the impact of a 100% uncertainty in the emissions, and if sampled at the observation locations, a crude approximation of the (square root of) the diagonal of $\mathbf{H}^T \mathbf{B} \mathbf{H}$.

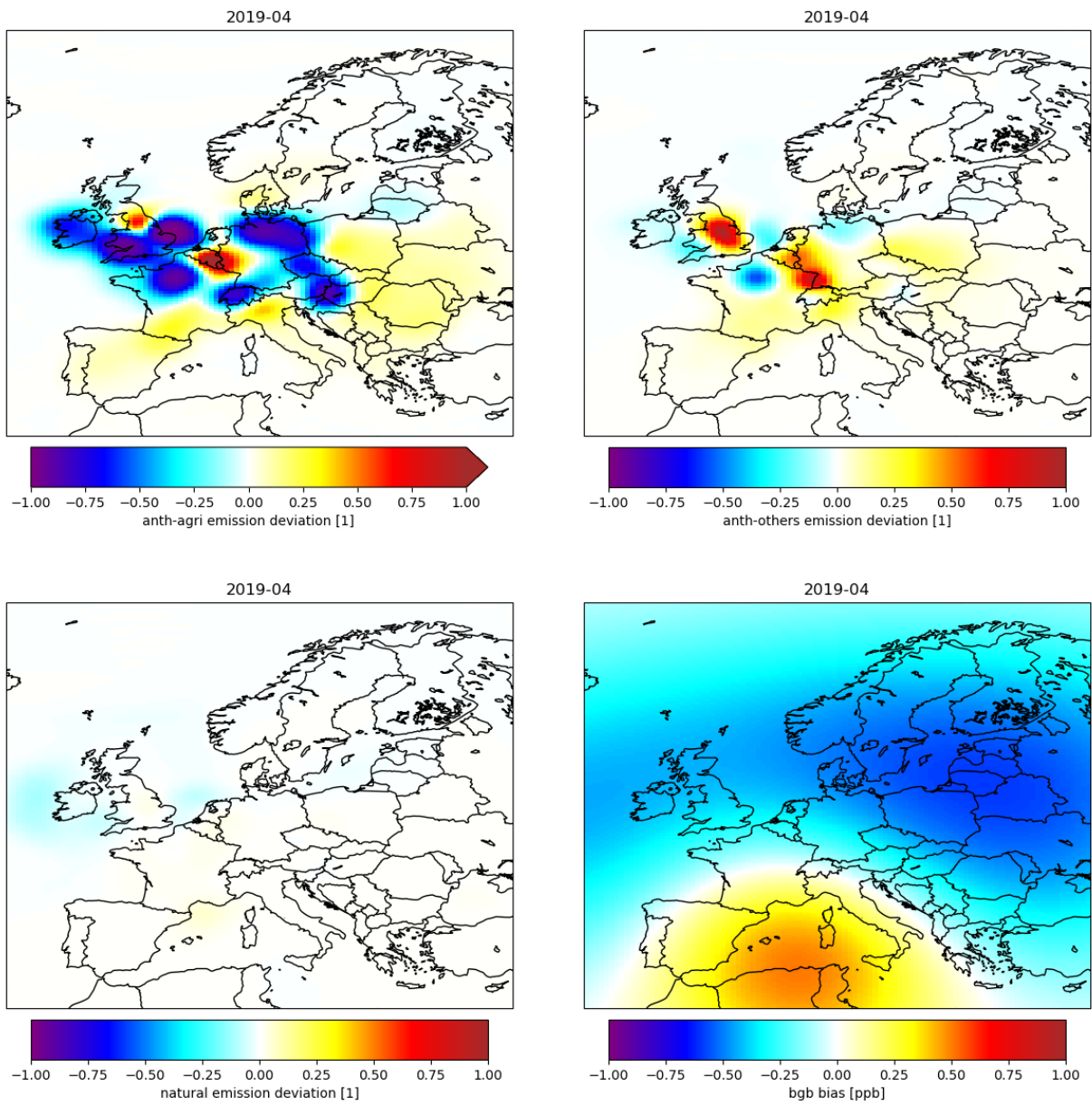


Figure 5: Example of optimized 2D correction fields in the 4D-var state.

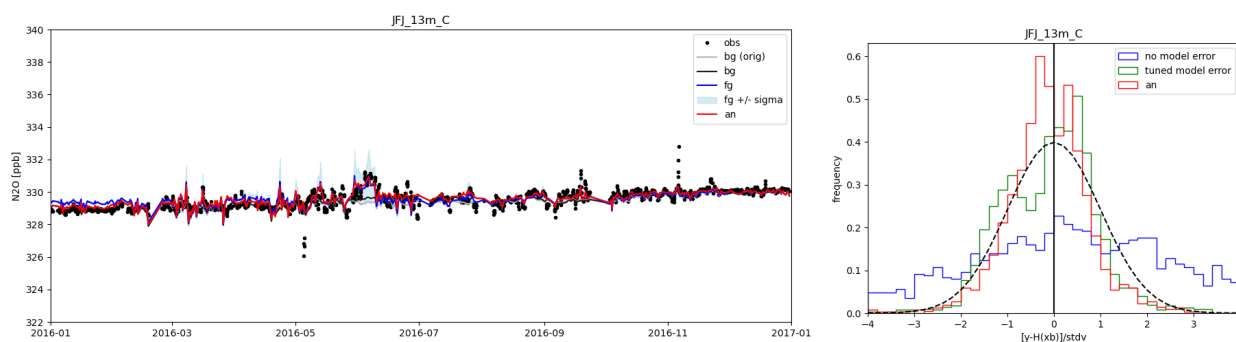


Figure 6: Illustration of tuning of the remaining observation representation error. The time series on the left for station Jungfraujoch shows an observations (black) and prior simulations (blue), where the shaded area denotes the 0-200% emission range. The histograms on the left are obtained from the observation-minus-simulation statistics; blue with only the instrumental error, and green with tuned remaining error. The dashed blue line show standard normal distribution. The red lines show the posterior simulations an statistics.

The parameters α are defined to represent the *remaining* representation error standard deviation in Eq. (6) for a single station in a specific year. To choose a suitable value, first all observations and simulations for a station in the specific year are collected, as well as the approximation of the variance due to emission uncertainties, and the assumed instrumental error. Together these can be used to evaluate the fractions in the left hand side of Eq. (8), and over these the sample standard deviation could be computed as a function of $r_{remaining}$. The remaining observation representation error is then set to a value that brings the sample standard deviation as close to one as possible. For some locations and years, the optimal value is actually zero, if the assumed emission uncertainties and instrumental errors are already able to explain most of the variation in observation-minus-simulation values.

The procedure is illustrated in Figure 6 using histograms of the observation-minus-simulation statistics. When the *remaining* representation error is not taken into account (blue histogram), the histogram of the statistics is too broad compared to the idealized standard normal distribution, which indicates that the assumed uncertainties are too small. After tuning (green), the histogram is in much better agreement with the expected normal distribution.

Note that the tuned observation representation errors only take into account uncertainty in emissions. The uncertainty in the background, as will be described in section 4.2.5, was not used when obtaining these values. It is therefore likely that the tuned values are actually too large, as a substantial portion of the model error is now actually assigned to the representation error.

4.2.5 Background correction

The baseline of the simulated N₂O mixing ratios is strongly defined by the global background values. For the LOTOS-EUROS simulations here, the 3D background fields from the global CAMS emission inversion are used for the years 2010-2022, as described in section 3.2. For 2023, the values from 2022 are used again after adding 1.12 ppb to account for the global increasing trend in the CAMS

data for that year.

Although based on an emission inversion, the background values have uncertainty too, for example because of their coarse resolution of about 100 km. In addition, also the way in which the LOTOS-EUROS model transports the background from the boundaries of the domain to the observation sites has errors. To compensate for all possible uncertainties, the 4D-Var state includes a *background correction* field δc that is therefore optimized too. Without this, the emissions might be adjusted to compensate for errors in the background values.

Compared to the emission uncertainties, the background correction is assumed to be less variable, with much longer spatial and temporal correlation length scales. To obtain suitable parameters for the covariance defined for δc , first all observations and simulations have been collected that are mainly representative for the background. This is done by selecting only the simulations where the impact of emissions is less than 0.05 ppb. Some sites are for a large part of the time representative for the background, in particular Mace Head (Ireland), Pallas (Finland), and Jungfraujoch (Switzerland). As example, the selected flask observations for station Mace Head (Ireland) are shown in the top panel of Figure 7. The standard deviation of these differences is small; over all samples, a value of 0.30 ppb seems representative and this has therefore been used for the entire field.

For each site, and if enough samples could be collected, the autocorrelation of the observation-minus-simulation values is computed too. These values show a decay with the time lag between the samples, as shown in the lower left panel of Figure 7. This decay is a suitable choice for the temporal correlation length scale τ from Eq. (4). Therefore, curves with exponential decay are fitted through the autocorrelation samples, in order to obtain estimates for τ . Based on the sites that are mainly representative for the background, a value of 3 months seems suitable.

Similar, a spatial correlation length scale L as in Eq. (3) could be estimated using the correlation between observation-minus-simulation values as function of distance. As not too many sites have very long time series with observations representative for background conditions, these statistics are rather noisy, as illustrated in the lower right panel of Figure 7. However, based on the statistics between the aforementioned three stations, a value of 1,200 km seems a suitable choice for L .

4.3 Comparison of setups

Although CIF-ICON-ART and LOTOS-EUROS use the same input data (background concentrations, prior fluxes, and assimilated observations), their inversion setups differ slightly. The main distinction lies in how each system prescribes the observation and prior errors, and optimize the background concentrations.

Table 1 summarizes the time-averaged prescribed mismatches for each inversion system. When averaged over the continuous observations, which represent 97% of the assimilated dataset, LOTOS-EUROS assigns a mean model–data mismatch of 0.49 ppb, almost identical to the value of 0.50 ppb used in CIF-ICON-ART. For most stations ($\sim 82\%$), the prescribed mismatch is slightly larger in CIF-ICON-ART. However, LOTOS-EUROS assigns substantially larger mismatches at BIK and CMN compared with CIF-ICON-ART, which offsets the generally lower values at other stations and brings the overall mean in line with that of CIF-ICON-ART. Consequently, apart from these two stations, LOTOS-EUROS places slightly greater confidence in the observational constraints. Assuming com-

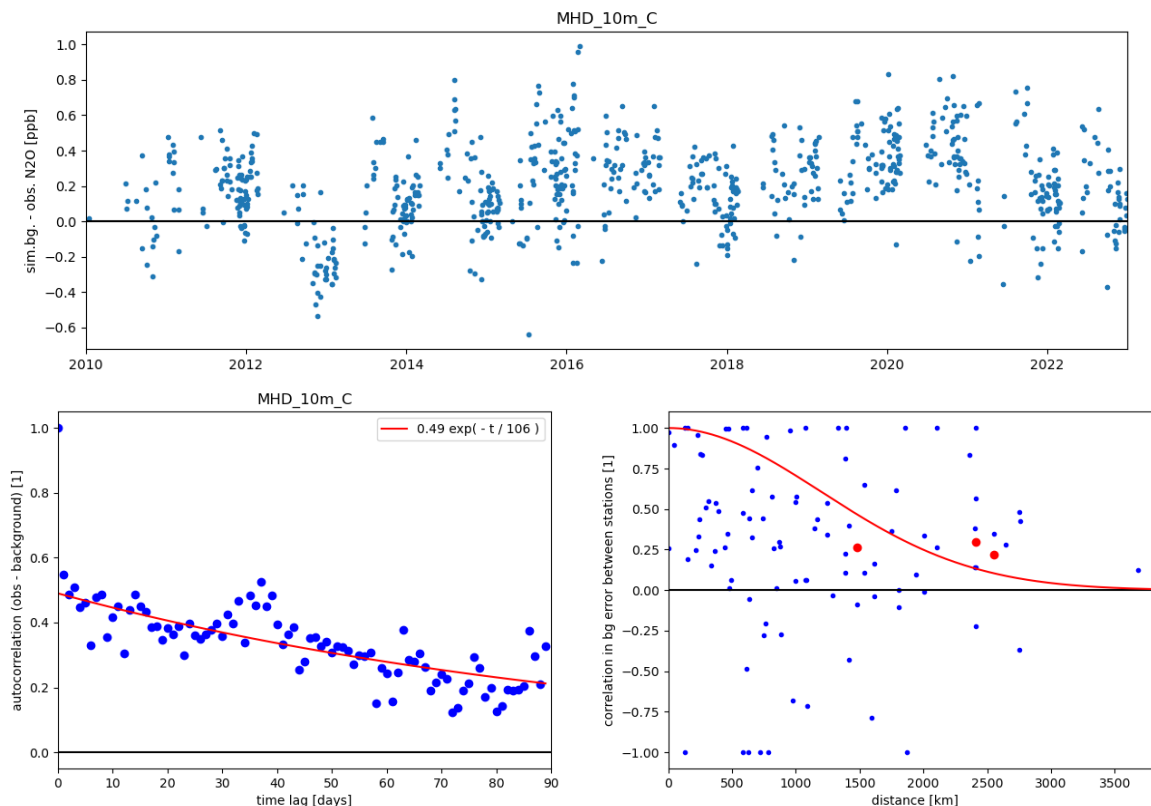


Figure 7: Top: timeseries of observation-minus-background values for station Mace Head that are representative for the background. Lower left: temporal autocorrelation with curve fitted. Lower right: spatial correlation between stations, with the red dots denoting the values between pairs out of Mace Head, Pallas, and Jungfrauoch.

parable model performance (prior fit to the observations), this should lead to a better posterior fit to the observations for LOTOS-EUROS.

A comparison of the parameters used to construct the prior-error covariance matrices is provided in Table 2. While the prescribed relative prior uncertainties for all emission categories are identical in both systems, CIF-ICON-ART assigns a larger prior uncertainty to the background. Analysis of the inversion results shows that the maximum background correction applied by CIF-ICON-ART is only 0.15% (~ 0.5 ppb). This suggests that prescribing a background uncertainty larger than about 0.5 ppb is unlikely to influence the outcome.

In both systems, emissions are optimized at the grid-cell scale. However, the background is optimized over 32 inflow regions in CIF-ICON-ART, whereas LOTOS-EUROS optimizes background concentrations at the grid-cell scale. In addition, LOTOS-EUROS prescribes smaller spatial and temporal correlation lengths for both emissions and background. This generally allows for greater spatial and temporal variability in the corrections.

Overall, LOTOS-EUROS has greater flexibility in adjusting the optimized variables.

5 Results

This section presents an analysis and comparison of the results provided by CIF-ICON-ART and LOTOS-EUROS.

5.1 Prior and posterior mole fractions

The inversion process aims to improve the fit between simulated and observed N₂O mole fractions. Figure 8 illustrates this for the Beromünster (BRM) station in 2022 for both inversion systems. The inversions substantially enhance the agreement between simulations and observations: correlations increase from 0.63 to 0.88 for CIF-ICON-ART and from 0.50 to 0.75 for LOTOS-EUROS. RMSE and mean bias are also reduced, and peaks as well as short-term variability are more accurately reproduced.

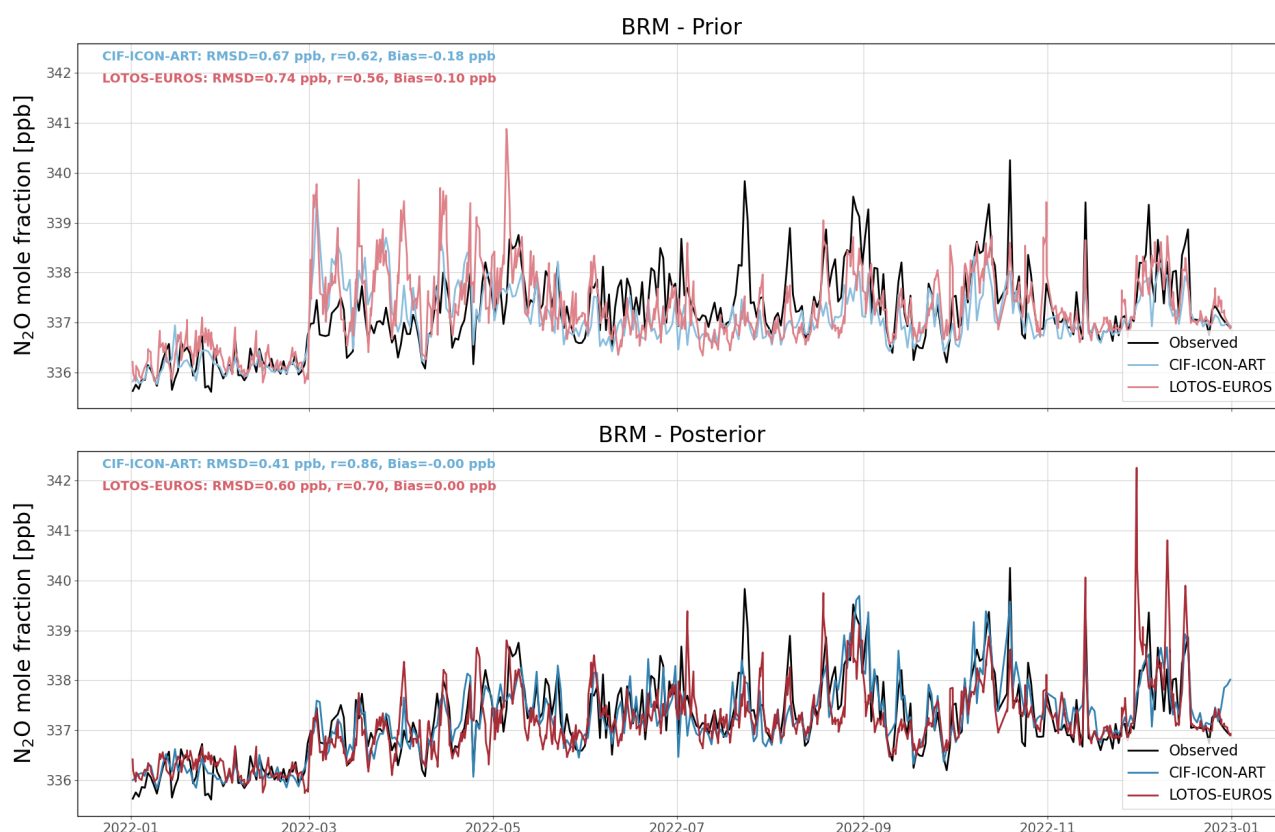


Figure 8: Example of observed and simulated N₂O mole-fraction time series at the Beromünster (BRM) station in 2022. Prior mole fractions from all inversion systems are shown in the upper panel, while the lower panel displays the posterior mole fractions. For each inversion system, the RMSE, Pearson correlation coefficient (r), and mean bias are listed in the upper-left corner of the respective panel.

These conclusions hold consistently across all assimilated stations (Fig. 9). Posterior correlations

are always higher than prior ones, and posterior RMSE values are systematically lower. Mean biases are generally reduced when their absolute value exceeds 0.5 ppb. However, some sites, such as Monte Cimone (CMN) and Lutjewad (LUT), retain substantial biases. LUT is particularly challenging for transport models, as reflected in its high RMSE and low correlation. Its location directly behind the Wadden Sea dike on the northern Dutch coast makes it sensitive to land–sea-breeze circulations and local turbulent flows that are difficult to resolve at the horizontal resolution (~ 25 km) of both models. The dike itself represents a sharp, sub-grid topographic feature that can influence turbulence and mixing, and complicate the representation of these processes in the model.

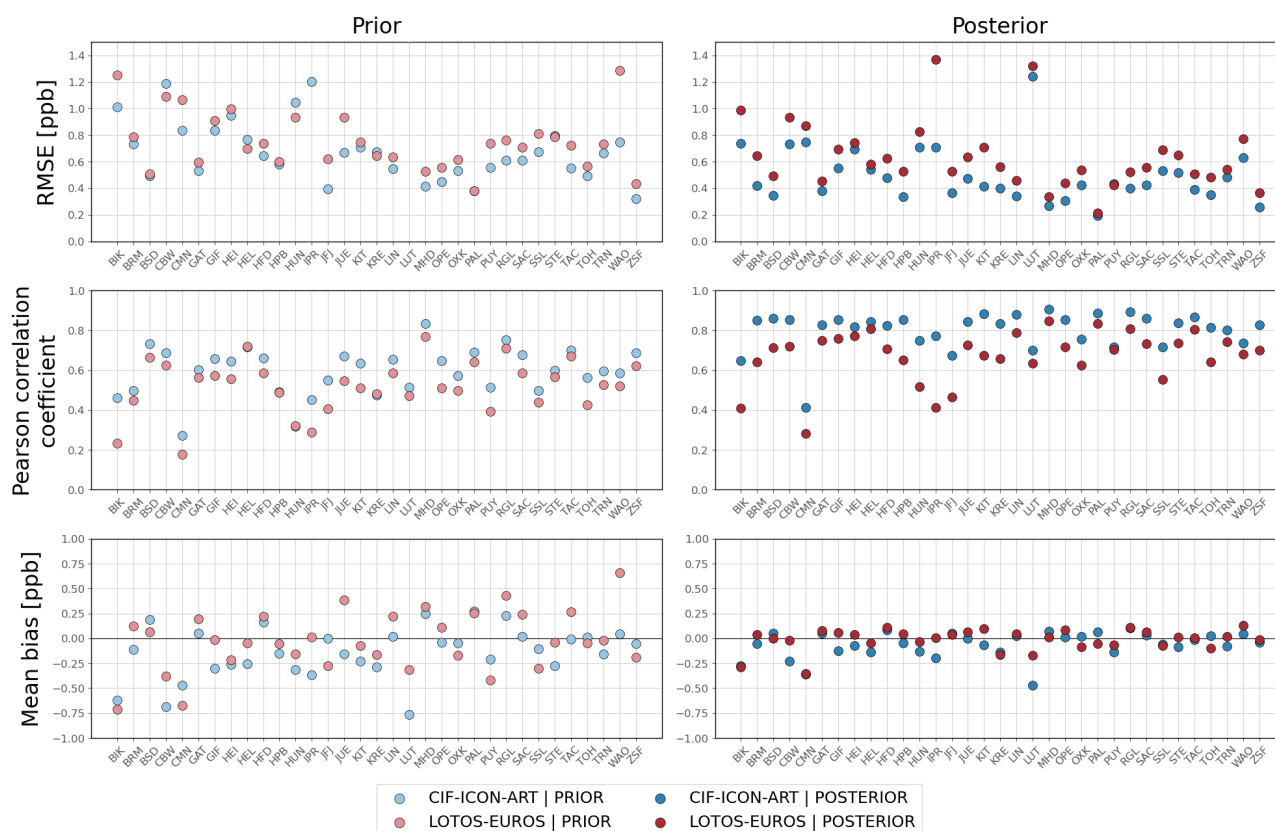


Figure 9: Root-mean-square error (RMSE), Pearson correlation coefficient, and mean bias computed for each station for the period 2010–2023. Time-series are detrended before computing the statistics. Prior results are shown in the left panels and posterior results in the right panels. Light colors corresponds to prior values, while dark colors indicates posterior values.

LOTOS-EUROS tends to reduce mean bias more effectively than CIF-ICON-ART, likely because its background optimization is performed independently for each grid cell, whereas CIF-ICON-ART uses only 32 inflow regions. While a larger number of degrees of freedom can reduce bias, it also increases the risk of overfitting. Conversely, too few regions may lead to underfitting. Importantly, because the number of N₂O monitoring stations in Europe is small (especially before 2019), no sites

were retained for independent validation. As a consequence, it is not possible to assess which system performs better outside the training domain.

Regarding RMSE and correlation, CIF-ICON-ART outperforms LOTOS-EUROS at nearly all stations in both prior and posterior simulations, providing more confidence in the flux adjustments derived by CIF-ICON-ART. Figure 10 presents the corresponding Taylor diagrams. In the prior, the overall correlation (computed from detrended time series) reaches 0.67 for CIF-ICON-ART, slightly higher than the 0.57 obtained with LOTOS-EUROS, although LOTOS-EUROS captures the observed variability better. After the inversion, the performance gap widens: posterior correlations increase to 0.85 for CIF-ICON-ART and 0.73 for LOTOS-EUROS, and both systems represent the observed variability similarly well. The stations IPR, WAO and CMN emerge as outliers in the diagrams, especially for LOTOS-EUROS.

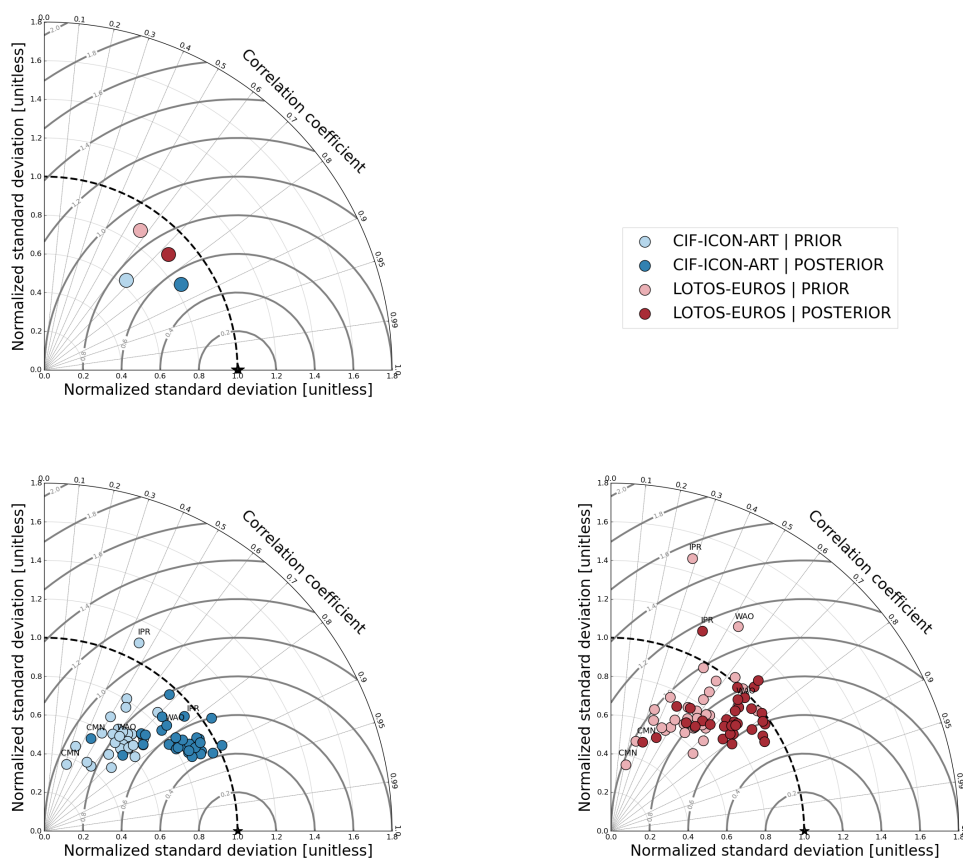


Figure 10: Normalized Taylor diagrams for the period 2010–2023 with detrended data. Each panel displays the performance of a different inversion system, with the exception of the upper-left panel, which compares the systems using aggregated metrics. Time-series are detrended before computing the statistics. In the upper-left panel, each marker represents the correlation and normalized standard deviation calculated over all observations. In the lower panels, markers correspond to individual stations. Light colors denote prior results, whereas dark colors denote posterior results.

5.2 Flux adjustments

To illustrate how mean biases simulated by the transport models relate to the flux adjustments derived by the inversion systems, we show the spatial distribution of the prior (background-corrected) mean bias in 2023, aggregated by quarter (Fig. 11), alongside the corresponding flux adjustments between the prior and posterior estimates (Fig. 12). Together, these figures clarify why the posterior fluxes differ between the two inversion systems: biases in the simulated mole fractions at the monitoring stations translate directly into the inferred flux adjustments. Positive model biases typically lead to reduced emissions, whereas negative biases result in increased emissions.

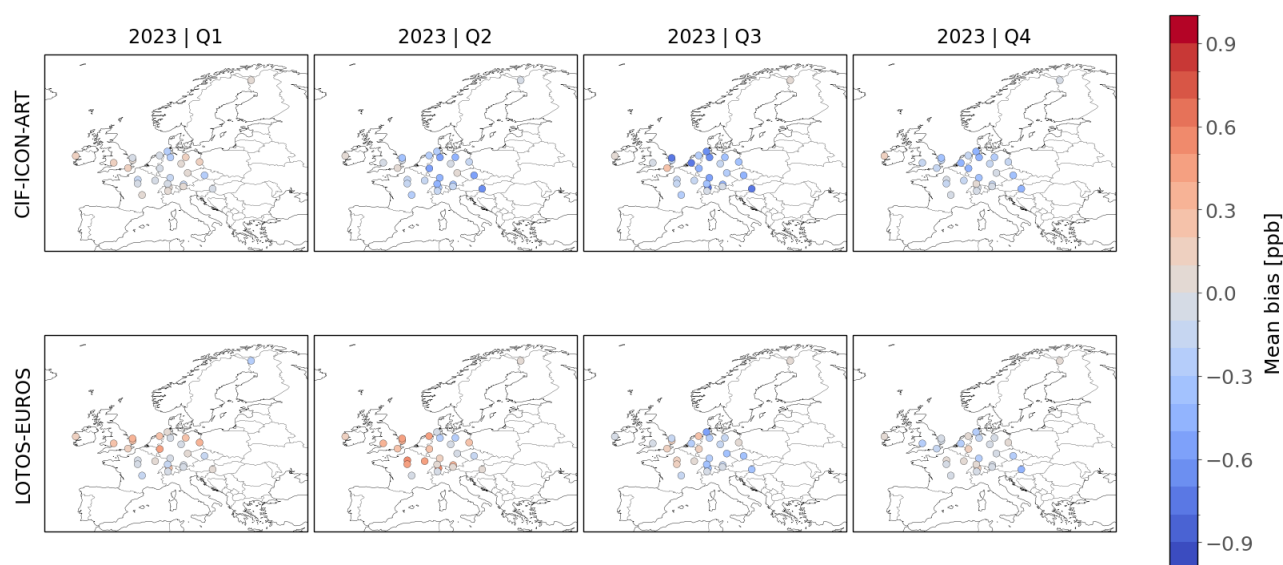


Figure 11: Mean bias between prior and observed N_2O mole fractions for all stations in 2023. Each column represents a different quarter of the year, while each row corresponds to a different inversion system. Before computing the bias, simulated mole fractions are corrected to remove the influence of background correction, by adding the difference between the prior simulated

The second quarter (April–June) shows the strongest divergence between the systems in 2023. CIF-ICON-ART infers a substantial emission increase over the Benelux region, consistent with the negative biases simulated there, and a modest decrease over the United Kingdom (UK). In contrast, LOTOS-EUROS produces a much larger emission reduction over the UK, reflecting its larger simulated biases, and derives a mixture of positive and negative flux corrections over the Benelux region to address those biases. The shorter correlation length prescribed for LOTOS-EUROS likely contributes to these discrepancies relative to CIF-ICON-ART.

When averaged over the full year 2023, CIF-ICON-ART infers a strong emission increase over the Benelux region, a small increase over Germany and the Czech Republic, and a small decrease over the UK (Fig. 13). Most of these patterns remain consistent across years, except for the UK, where adjustments alternate between small increases and decreases, and France, where adjustments range from negligible to slightly positive. Overall, CIF-ICON-ART indicates that prior emissions

in national inventories are underestimated across most regions, especially in the Benelux region. LOTOS-EUROS, however, produces adjustments that differ markedly from those of CIF-ICON-ART: emissions over the Netherlands are almost always increased, emissions over Belgium tend to be decreased, and France and Germany exhibit regionally varying patterns. Over the UK, LOTOS-EUROS consistently infers emission decreases, yielding posterior estimates that align more closely with the national inventories. As a result, substantial spatial discrepancies emerge between the two inversion systems, driven primarily by differences in prescribed correlation lengths and simulated biases at the monitoring stations. The only consistent feature across both systems is the increase over the Netherlands, which hosts one of the most intensive agricultural systems in the world.

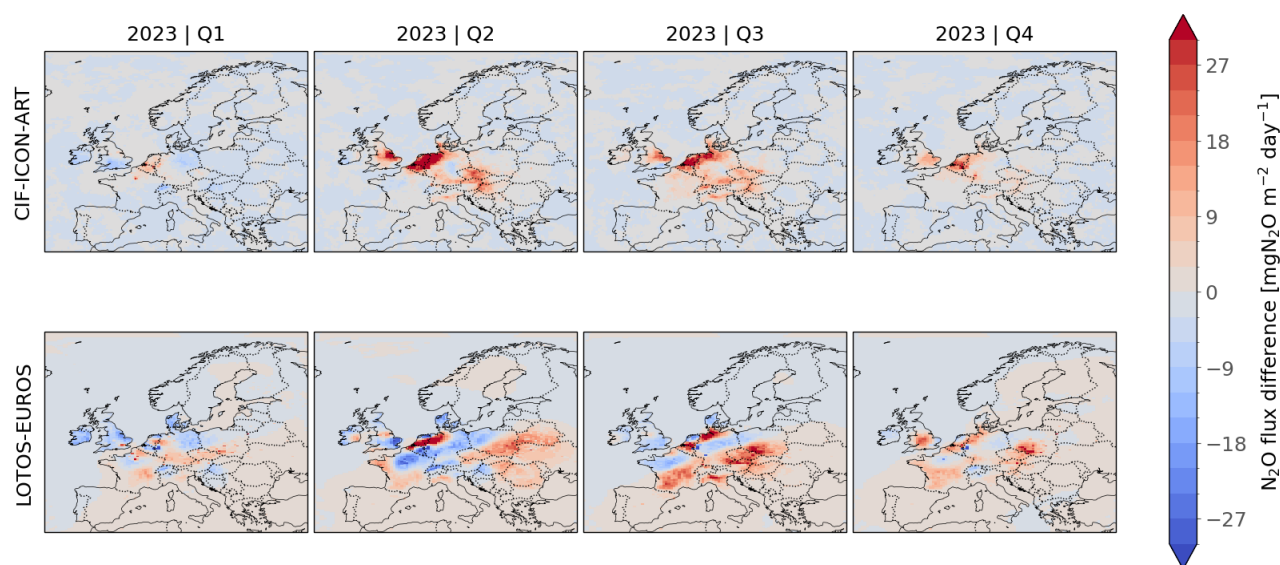


Figure 12: Maps of N_2O flux adjustments for 2023. Flux adjustments are defined as the difference between posterior and prior fluxes. Each column represents a different quarter of the year, while each row corresponds to a different inversion system.

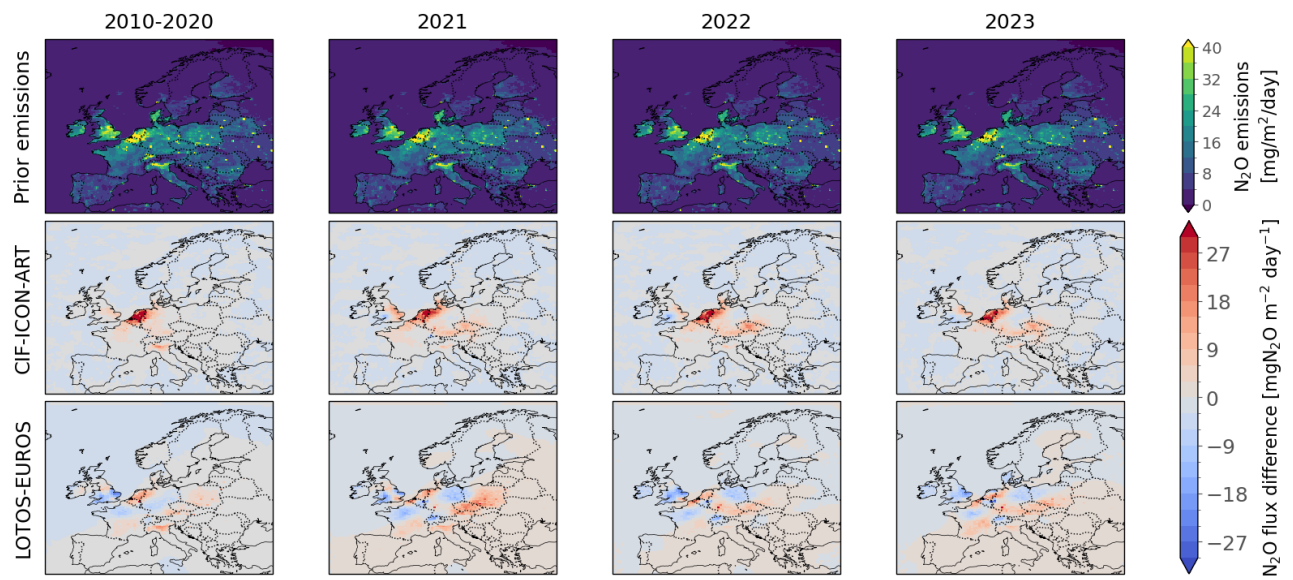


Figure 13: Maps of N_2O prior fluxes and flux adjustments across different periods and years. Flux adjustments are defined as the difference between posterior and prior fluxes. Each column corresponds to a specific period or year. The first row shows the prior N_2O emissions, and each subsequent row corresponds to the flux adjustments derived a different inversion system.

5.3 Analysis of posterior fluxes

The analysis of monthly posterior fluxes for the various European countries and regions reveals a consistent re-evaluation of the seasonal cycle (Fig. 14). When aggregated over EU27+ (EU27 plus the United Kingdom, Switzerland, and Norway), the emission peak shifts from March (with March, April and May showing similar flux levels) in the prior estimates to May in the posterior estimates, with a clear maximum occurring in this month. This shift appears robust across years and regions and is reproduced by both CIF-ICON-ART and LOTOS-EUROS, underscoring the consistency of the revised seasonal pattern.

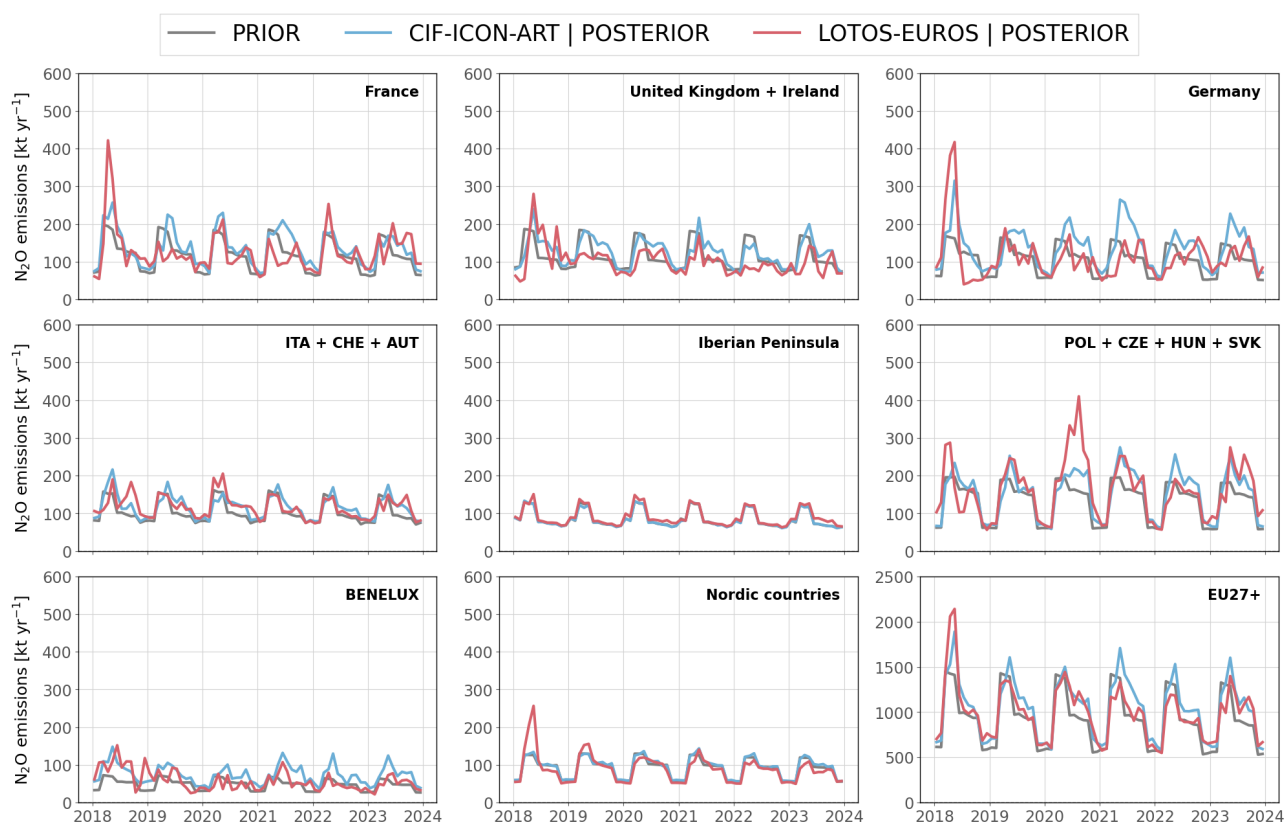


Figure 14: Time-series of monthly total N₂O emissions (2017–2023) for multiple European countries and regions. The time-series starts in 2018 for better readability. Regional groupings are: ITA+CHE+AUT (Italy, Switzerland, Austria), POL+CZE+HUN+SVK (Poland, Czechia, Hungary, Slovakia), Benelux (Belgium, Netherlands, Luxembourg), Nordic countries (Norway, Sweden, Finland, Denmark), and EU27+ (EU27 plus United Kingdom, Switzerland and Norway).

Additionally, another smaller peak emerges in September–October for some regions (e.g., EU27+, Benelux, France, Germany, Eastern Europe), also reasonably consistent between the two inverse systems. Spring is one of the main periods for applying synthetic nitrogen fertilizer and manure. Consequently, the first peak likely results from the combination of high soil moisture, rising temperatures, and substantial nitrogen inputs, all of which stimulate microbial activity and enhance N₂O

production. The second peak occurs under similarly favorable conditions, with soils remaining warm and often moist in early autumn. In this period, nitrogen inputs may arise either from additional synthetic fertilizer or manure applications or from the decomposition of crop residues incorporated into the soil.

Analysis of annual emissions (Fig. 15) reveals clear differences between LOTOS-EUROS and CIF-ICON-ART. As mentioned above, CIF-ICON-ART increases emissions relative to the prior in nearly all regions, whereas LOTOS-EUROS produces estimates that align more closely with the national inventories, although they are also slightly larger. Averaged over 2010–2023, N₂O anthropogenic emissions in EU27+ are estimated at 986 ktN₂O yr⁻¹ by CIF-ICON-ART and 925 ktN₂O yr⁻¹ by LOTOS-EUROS, while the prior emissions are estimated at of 868 ktN₂O yr⁻¹. Between the periods 2010–2019 and 2020–2023, CIF-ICON-ART and LOTOS-EUROS both infer reductions of 44 and 73 ktN₂O yr⁻¹, respectively. Overall, the emissions derived by CIF-ICON-ART are slightly more stable (standard deviation equal to 30 ktN₂O yr⁻¹) than those obtained with LOTOS-EUROS (standard deviation equal to 38 ktN₂O yr⁻¹). Strangely, LOTOS-EUROS exhibits a pronounced peak in 2018, driven mainly by elevated emissions in the Benelux region, France, Germany, and Eastern Europe, that are difficult to interpret and not supported by CIF-ICON-ART. CIF-ICON-ART infers a substantial increase in emissions over the Benelux region between 2013 and 2019. This increase appears to be an artefact of the system. Before background correction, the prior bias differs strongly between the Benelux region (LUT and CBW stations) and the other regions. Consequently, the background correction reduces biases at the other stations but not at LUT and CBW, forcing the flux adjustments to compensate. Although the origin of the large simulated biases at LUT and CBW is still unclear during this period, allowing greater flexibility in the background optimization, similar to the approach used by LOTOS-EUROS, may help to resolve this issue in future inversions.

CIF-ICON-ART indicates a notable increase in emissions in 2021 followed by a marked decrease in 2022. These variations are consistent with the meteorological conditions of those years: spring and summer 2021 were unusually wet across much of Europe, increasing soil moisture and enhancing microbial N₂O production. The increased precipitation in 2021 may have also raised soil moisture to levels that inhibit N₂O production, potentially explaining this difference with LOTOS-EUROS, which infers reduced emissions in 2021. On the opposite, the widespread drought of 2022 likely suppressed microbial activity and reduced emissions, which is both captured by LOTOS-EUROS and CIF-ICON-ART. In 2023, temperatures were higher and precipitation levels increased relative to 2022, resulting in fewer drought events and more stable conditions. Both systems detect a rise in emissions compared with the previous year.

CIF-ICON-ART was the only system capable of providing posterior uncertainties, which are also shown in Figure 15. Besides a few years and regions, the LOTOS-EUROS estimates fall well within the uncertainty range (one standard deviation) derived by CIF-ICON-ART. For most regions, the uncertainty reaches a maximum in 2016, when the number of N₂O monitoring stations was at its lowest (13), and decreases thereafter, reaching a minimum in 2021, when the number of stations was highest (28). This highlights the critical role of observational coverage in improving the robustness of flux estimates. France, the UK, Germany, and the Benelux region show the largest reductions in uncertainty, reflecting the concentration of monitoring stations in Western Europe. The greatest

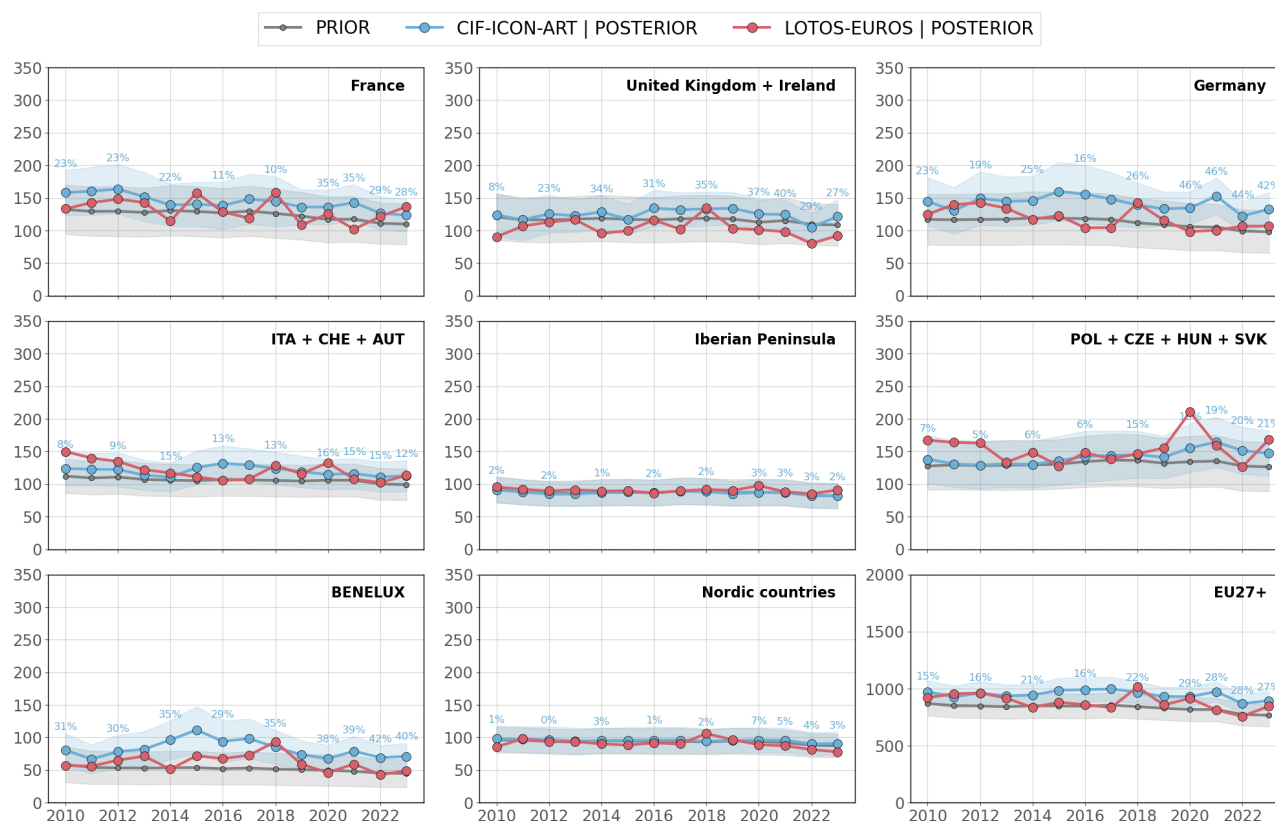


Figure 15: Time-series of annual total N₂O emissions (2010–2023) for multiple European countries and regions. Regional groupings are: ITA+CHE+AUT (Italy, Switzerland, Austria), POL+CZE+HUN+SVK (Poland, Czechia, Hungary, Slovakia), Benelux (Belgium, Netherlands, Luxembourg), Nordic countries (Norway, Sweden, Finland, Denmark), and EU27+ (EU27 plus United Kingdom, Switzerland and Norway). The shaded grey and blue areas represent the prior and posterior uncertainties prescribed and derived by CIF-ICON-ART (1 standard deviation), respectively. For some years, the relative uncertainty reduction is displayed on top of the shaded area. The relative uncertainty reduction is defined as the relative difference between the posterior and prior relative uncertainties. LOTOS-EUROS could not provide posterior uncertainties.

relative reduction occurs in Germany, where posterior uncertainties in recent years are nearly half of the prior values. Across EU27+, relative uncertainties are reduced by roughly 25% in recent years, underscoring the importance of combining bottom-up approaches with inverse modeling to obtain robust flux estimates. Posterior uncertainties also allow to infer that there was no statistically significant positive or negative trend between 2010 and 2023 for any region in Europe.

The spatial anomalies, shown in Figure 16, are inconsistent between LOTOS-EUROS and CIF-ICON-ART for the year 2021. While LOTOS-EUROS derives a strong decrease of emissions in France and in Northern Germany compared to 2010–2020, CIF-ICON-ART mainly finds an increase in Czech Republic, in Poland and a decrease in the Benelux region. Anomalies in 2022 are more consistent, with a strong decrease over the Benelux region, in the UK, and in Northern Germany.

However, anomalies of opposite signs emerge over Southern Germany, Czech Republic and Poland. For 2023, EU₂₇₊ emissions are comparable across models, but notable spatial discrepancies remain, especially in the Benelux region and in southern Germany and France. These discrepancies are likely explained by the different spatial correlation lengths prescribed and the differences in simulated biases.

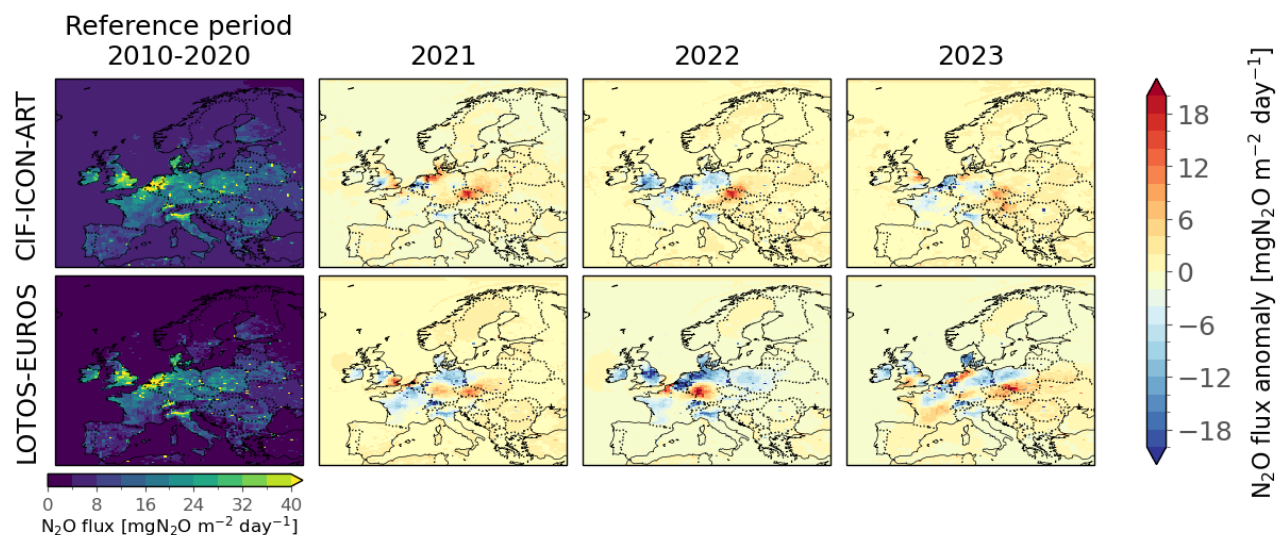


Figure 16: Maps of annual N₂O emission anomalies for recent years relative to a reference period (2010–2020). Each column shows the annual anomaly for a given year, except for the first column, which presents the mean emissions over the reference period. Each row represents a different inversion system.

The two inversion systems optimized the three emission categories separately, therefore allowing the modification of their respective contributions to total emissions. Figure 17 shows the evolution of these contributions over time for several regions. The two systems have opposite outcomes. While CIF-ICON-ART generally increases the contributions from agricultural emissions by a few percents for all regions, compared to the prior, while LOTOS-EUROS does the opposite, decreasing the contributions from agricultural emissions and increase the ones from other anthropogenic emissions. For example, CIF-ICON-ART shifts agricultural emissions over UK from 64% in the prior, to 65%, while LOTOS-EUROS reduces it to 57%. Over the whole EU₂₇₊, the opposite conclusions remain but the contributions inferred by the two systems differ by only 1-2%. Regarding temporal trends, CIF-ICON-ART indicates a gradual increase in the agricultural contribution, consistent with the prior estimates, across nearly all regions. In contrast, LOTOS-EUROS produces more variable proportions. For instance, in the Benelux region, agricultural emissions account for 69% in 2010, 57% in 2014, 62% in 2018, 74% in 2020, and 83% in 2023.

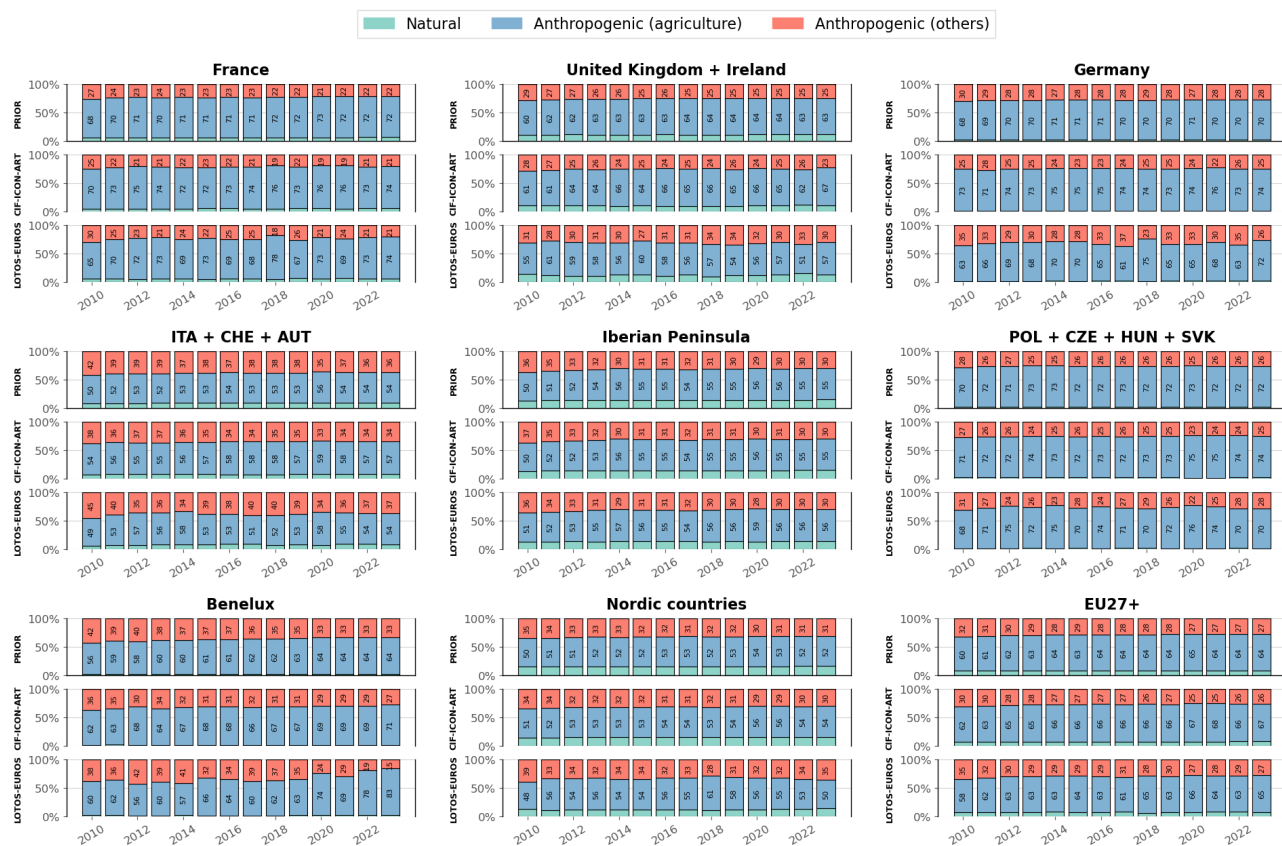


Figure 17: Time series of annual contributions from each emission category to total emissions for several European countries and regions. Regional groupings are defined as follows: ITA+CHE+AUT (Italy, Switzerland, Austria), POL+CZE+HUN+SVK (Poland, Czechia, Hungary, Slovakia), Benelux (Belgium, the Netherlands, Luxembourg), Nordic countries (Norway, Sweden, Finland, Denmark), and EU27+ (EU27 plus the United Kingdom, Switzerland, and Norway). For each region, the top panel shows prior emissions, while the remaining panels display posterior emissions derived from different inversion systems. The contribution of each category is indicated within its respective bar.

6 Discussion and conclusion

This report presents and analyzes N₂O inversion results over Europe obtained with two inversion systems, CIF-ICON-ART and LOTOS-EUROS. This work enabled Empa and TNO to extend their inversion frameworks to the species N₂O and to perform top-down emission estimates of this new species for the first time.

Both systems indicate a need to reassess the seasonal peak, a reduction in emissions during 2020–2023 relative to 2010–2019, and broadly similar year-to-year variations in recent years. Notably, the results suggest that N₂O emissions in the most recent period were strongly influenced by extreme events (droughts, floods, heatwaves), whose frequency is increasing. However, the limited number of systems involved in this exercise, combined with the inconsistencies between their outputs, prevents us from drawing robust conclusions.

Nevertheless, following a strict common protocol enabled a meaningful comparison and helped explain most of the discrepancies between the estimates, showing that inversion setup and biases in the prior simulations have a dominant influence on differences in the posterior emissions. Moreover, the most recent years are much better constrained thanks to the sustained efforts of the measurement teams operating the European observational network. This improvement will make it possible to include dedicated validation stations in future studies to assess the performance of each inversion system outside the training domain. Continued investment in the observational network will be essential for deriving reliable long-term trends.

For future work, we strongly recommend conducting similar exercises with a larger ensemble of models and inversion systems.

References

- Berchet, A., Sollum, E., Thompson, R. L., Pison, I., Thanwerdas, J., Broquet, G., Chevallier, F., Aalto, T., Berchet, A., Bergamaschi, P., Brunner, D., Engelen, R., Fortems-Cheiney, A., Gerbig, C., Groot Zwaaftink, C. D., Haussaire, J.-M., Henne, S., Houweling, S., Karstens, U., Kutsch, W. L., Lujikx, I. T., Monteil, G., Palmer, P. I., van Peet, J. C. A., Peters, W., Peylin, P., Potier, E., Rödenbeck, C., Saunois, M., Scholze, M., Tsuruta, A., and Zhao, Y.: The Community Inversion Framework v1.0: A Unified System for Atmospheric Inversion Studies, *Geoscientific Model Development*, 14, 5331–5354, doi:10.5194/gmd-14-5331-2021, 2021.
- Bergamaschi, P., Segers, A., Brunner, D., Haussaire, J.-M., Henne, S., Ramonet, M., Arnold, T., Biermann, T., Chen, H., Conil, S., Delmotte, M., Forster, G., Frumau, A., Kubistin, D., Lan, X., Leuenberger, M., Lindauer, M., Lopez, M., Manca, G., Müller-Williams, J., O'Doherty, S., Scheeren, B., Steinbacher, M., Trisolino, P., Vítková, G., and Yver Kwok, C.: High-resolution inverse modelling of European CH₄ emissions using the novel FLEXPART-COSMO TM5 4DVAR inverse modelling system, *Atmospheric Chemistry and Physics*, 22, 13243–13268, doi:10.5194/acp-22-13243-2022, URL <https://acp.copernicus.org/articles/22/13243/2022/>, 2022.
- Calvo Buendia, E., Tanabe, K., Kranjc, A., Baasansuren, J., Fukuda, M., Ngarize, S., Osako, A., Pyrozhenko, Y., Shermanau, P., and Federici, S., eds.: 2019 Refinement to the 2006 IPCC Guidelines for National Greenhouse Gas Inventories, Intergovernmental Panel on Climate Change (IPCC), Switzerland, URL <https://www.ipcc.ch/report/2019-refinement-to-the-2006-ipcc-guidelines-for-national-greenhouse-gas-inventories/>, published by the IPCC, Geneva, Switzerland, 2019.
- Chevallier, F. and Thompson, R.: Evaluation and Quality Control Document for Observation-Based N₂O Flux Estimates for the Period 1996-2022, 2024.
- Dröge, R., van Mil, S., Super, I., Denier van der Gon, H., Brunner, D., Constantin, L., Karstens, U., Wu, Z., Lagergren, F., Scholze, M., Lundblad, M., Witt, H., and van Zanten, M.: AVENGERS Deliverable 2.2: Anthropogenic Emission Inventories and Natural Flux Data Sets, Project deliverable, 2024.
- Forster, P., Storelvmo, T., Armour, K., Collins, W., Dufresne, J.-L., Frame, D., Lunt, D. J., Mauritsen, T., Palmer, M. D., Watanabe, M., Wild, M., and Zhang, H.: The Earth's Energy Budget, Climate Feedbacks, and Climate Sensitivity, in: *Climate Change 2021: The Physical Science Basis. Contribution of Working Group I to the Sixth Assessment Report of the Intergovernmental Panel on Climate Change*, edited by Masson-Delmotte, V., Zhai, P., Pirani, A., Connors, S. L., Péan, C., Berger, S., Caud, N., Chen, Y., Goldfarb, L., Gomis, M. I., Huang, M., Leitzell, K., Lonnoy, E., Matthews, J. B. R., Maycock, T. K., Waterfield, T., Yelekçi, O., Yu, R., and Zhou, B., pp. 923–1054, Cambridge University Press, Cambridge, United Kingdom and New York, NY, USA, doi:10.1017/9781009157896.009, 2021.
- Heiskanen, J., Brümmer, C., Buchmann, N., Calfapietra, C., Chen, H., Gielen, B., Gkritzalis, T., Hammer, S., Hartman, S., Herbst, M., Janssens, I. A., Jordan, A., Juurola, E., Karstens, U.,

- Kasurinen, V., Kruijt, B., Lankreijer, H., Levin, I., Linderson, M.-L., Loustau, D., Merbold, L., Myhre, C. L., Papale, D., Pavelka, M., Pilegaard, K., Ramonet, M., Rebmann, C., Rinne, J., Rivier, L., Saltikoff, E., Sanders, R., Steinbacher, M., Steinhoff, T., Watson, A., Vermeulen, A. T., Vesala, T., Vítková, G., and Kutsch, W.: The Integrated Carbon Observation System in Europe, doi:10.1175/BAMS-D-19-0364.1, 2022.
- Henne, S., Brunner, D., Oney, B., Leuenberger, M., Eugster, W., Bamberger, I., Meinhardt, F., Steinbacher, M., and Emmenegger, L.: Validation of the Swiss methane emission inventory by atmospheric observations and inverse modelling, *Atmospheric Chemistry and Physics*, 16, 3683–3710, doi:10.5194/acp-16-3683-2016, URL <https://acp.copernicus.org/articles/16/3683/2016/>, 2016.
- Henne, S., Arduini, J., Arnold, T., Barcza, Z., Bergamaschi, P., Chen, H., Colomb, A., Conil, S., Couret, C., Cuevas-Agulló, E., Emmenegger, L., Forster, G., Frumau, A., Hammer, S., Haszpra, L., Hatakka, J., Hensen, A., Hoheisel, A., Kneuer, T., Komínková, K., Kubistin, D., Lan, X., Laurent, O., Lavrič, J., Leuenberger, M., Levin, I., Lindauer, M., Lopez, M., Manca, G., Marek, M. V., Meinhardt, F., Müller-Williams, J., O'Doherty, S., Pichon, J.-M., Plaß-Dülmer, C., Ramonet, M., Rivas-Soriano, P., Scheeren, B., Schmidt, M., Steinbacher, M., Vítková, G., Yver-Kwok, C., Vermeulen, A., and Popa, E.: Collection of historic and ongoing N₂O observations across Europe (release 2024-11), doi:10.18160/JRG0-T7AJ, URL <https://meta.icos-cp.eu/collections/YYQEWAMzIT64LotSp9xXjqNt>, 2024.
- Hersbach, H., Bell, B., Berrisford, P., Hirahara, S., Horányi, A., Muñoz-Sabater, J., Nicolas, J., Peubey, C., Radu, R., Schepers, D., Simmons, A., Soci, C., Abdalla, S., Abellan, X., Balsamo, G., Bechtold, P., Biavati, G., Bidlot, J., Bonavita, M., De Chiara, G., Dahlgren, P., Dee, D., Diamantakis, M., Dragani, R., Flemming, J., Forbes, R., Fuentes, M., Geer, A., Haimberger, L., Healy, S., Hogan, R. J., Hólm, E., Janisková, M., Keeley, S., Laloyaux, P., Lopez, P., Lupu, C., Radnoti, G., de Rosnay, P., Rozum, I., Vamborg, F., Villaume, S., and Thépaut, J.-N.: Complete ERA5 from 1940: Fifth generation of ECMWF atmospheric reanalyses of the global climate, Copernicus Climate Change Service (C3S) Data Store (CDS), doi:10.24381/cds.143582cf, 2017.
- Hersbach, H., Bell, B., Berrisford, P., Hirahara, S., Horányi, A., Muñoz-Sabater, J., Nicolas, J., Peubey, C., Radu, R., Schepers, D., Simmons, A., Soci, C., Abdalla, S., Abellan, X., Balsamo, G., Bechtold, P., Biavati, G., Bidlot, J., Bonavita, M., De Chiara, G., Dahlgren, P., Dee, D., Diamantakis, M., Dragani, R., Flemming, J., Forbes, R., Fuentes, M., Geer, A., Haimberger, L., Healy, S., Hogan, R. J., Hólm, E., Janisková, M., Keeley, S., Laloyaux, P., Lopez, P., Lupu, C., Radnoti, G., de Rosnay, P., Rozum, I., Vamborg, F., Villaume, S., and Thépaut, J.-N.: The ERA5 global reanalysis, *Quarterly Journal of the Royal Meteorological Society*, 146, 1999–2049, doi:<https://doi.org/10.1002/qj.3803>, URL <https://rmets.onlinelibrary.wiley.com/doi/abs/10.1002/qj.3803>, 2020.
- Hersbach, H., Bell, B., Berrisford, P., Biavati, G., Horányi, A., Muñoz Sabater, J., Nicolas, J., Peubey, C., Radu, R., Rozum, I., Schepers, D., Simmons, A., Soci, C., Dee, D., and Thépaut,

- J.-N.: ERA5 hourly data on single levels from 1940 to present, Copernicus Climate Change Service (C3S) Climate Data Store (CDS), doi:10.24381/cds.adbb2d47, 2023.
- Hoshyaripour, G. A., Baer, A., Bierbauer, S., Bruckert, J., Brunner, D., Foerstner, J., Hamzehloo, A., Hanft, V., Keller, C., Klose, M., Kumar, P., Ludwig, P., Metzner, E., Muth, L., Pauling, A., Porz, N., Reddmann, T., Reißig, L., Ruhnke, R., Satitkovitchai, K., Seifert, A., Sinnhuber, M., Steiner, M., Versick, S., Vogel, H., Weimer, M., Werchner, S., and Hoose, C.: The Atmospheric Composition Component of the ICON modeling framework: ICON-ART version 2025.04, EGU sphere, doi:10.5194/egusphere-2025-3400, URL <https://doi.org/10.5194/egusphere-2025-3400>, [preprint], 2025.
- Jähn, M., Kuhlmann, G., Mu, Q., Haussaire, J.-M., Ochsner, D., Osterried, K., Clément, V., and Brunner, D.: An Online Emission Module for Atmospheric Chemistry Transport Models: Implementation in COSMO-GHG v5.6a and COSMO-ART v5.1-3.1, Geoscientific Model Development, 13, 2379–2392, doi:10.5194/gmd-13-2379-2020, 2020.
- Karstens, U.: AVENGERS Deliverable 2.1: Dataset on observations, Project deliverable, 2023.
- Kuenen, J., Dellaert, S., Visschedijk, A., Jalkanen, J.-P., Super, I., and Denier van der Gon, H.: CAMS-REG-v4: A State-of-the-Art High-Resolution European Emission Inventory for Air Quality Modelling, Earth System Science Data, 14, 491–515, doi:10.5194/essd-14-491-2022, 2022.
- Lan, X., Thoning, K. W., and Dlugokencky, E. J.: Trends in globally-averaged CH₄, N₂O, and SF₆ determined from NOAA Global Monitoring Laboratory measurements, doi:10.15138/P8XG-AA10, URL <https://doi.org/10.15138/P8XG-AA10>, 2022.
- Lan, X., Thoning, K. W., and Dlugokencky, E. J.: Trends in globally-averaged CH₄, N₂O, and SF₆ determined from NOAA Global Monitoring Laboratory measurements, Version 2025-11, doi:10.15138/P8XG-AA10, URL <https://doi.org/10.15138/P8XG-AA10>, 2025.
- Li, Y., Tian, H., Yao, Y., Shi, H., Bian, Z., Shi, Y., Wang, S., Maavara, T., Lauerwald, R., and Pan, S.: Increased Nitrous Oxide Emissions from Global Lakes and Reservoirs since the Pre-Industrial Era, Nature Communications, 15, 942, doi:10.1038/s41467-024-45061-0, 2024.
- Manders, A. M. M., Bultjes, P. J. H., Curier, L., Denier van der Gon, H. A. C., Hendriks, C., Jonkers, S., Kranenburg, R., Kuenen, J. J. P., Segers, A. J., Timmermans, R. M. A., Visschedijk, A. J. H., Wichink Kruit, R. J., van Pul, W. A. J., Sauter, F. J., van der Swaluw, E., Swart, D. P. J., Douros, J., Eskes, H., van Meijgaard, E., van Ulft, B., van Velthoven, P., Banzhaf, S., Mues, A. C., Stern, R., Fu, G., Lu, S., Heemink, A., van Velzen, N., and Schaap, M.: Curriculum vitae of the LOTOS–EUROS (v2.0) chemistry transport model, Geoscientific Model Development, 10, 4145–4173, doi:10.5194/gmd-10-4145-2017, URL <https://gmd.copernicus.org/articles/10/4145/2017/>, 2017.
- Petrescu, A. M. R., Qiu, C., McGrath, M. J., Peylin, P., Peters, G. P., Ciais, P., Thompson, R. L., Tsuruta, A., Brunner, D., Kuhnert, M., Matthews, B., Palmer, P. I., Tarasova, O., Regnier, P., Lauerwald, R., Bastviken, D., Höglund-Isaksson, L., Winiwarter, W., Etiope, G., Aalto, T.,

- Balsamo, G., Bastrikov, V., Berchet, A., Brockmann, P., Ciotoli, G., Conchedda, G., Crippa, M., Dentener, F., Groot Zwaftink, C. D., Guizzardi, D., Günther, D., Haussaire, J.-M., Houweling, S., Janssens-Maenhout, G., Kouyate, M., Leip, A., Leppänen, A., Lugato, E., Maisonnier, M., Manning, A. J., Markkanen, T., McNorton, J., Muntean, M., Oreggioni, G. D., Patra, P. K., Perugini, L., Pison, I., Raivonen, M. T., Saunois, M., Segers, A. J., Smith, P., Solazzo, E., Tian, H., Tubiello, F. N., Vesala, T., van der Werf, G. R., Wilson, C., and Zaehle, S.: The Consolidated European Synthesis of CH₄ and N₂O Emissions for the European Union and United Kingdom: 1990–2019, *Earth System Science Data*, 15, 1197–1268, doi:10.5194/essd-15-1197-2023, 2023.
- Remaud, M., Chevallier, F., Maignan, F., Belviso, S., Berchet, A., Parouffe, A., Abadie, C., Bacour, C., Lennartz, S., and Peylin, P.: Plant Gross Primary Production, Plant Respiration and Carbonyl Sulfide Emissions over the Globe Inferred by Atmospheric Inverse Modelling, *Atmospheric Chemistry and Physics*, 22, 2525–2552, doi:10.5194/acp-22-2525-2022, 2022.
- Resplandy, L., Hogikyan, A., Müller, J. D., Najjar, R. G., Bange, H. W., Bianchi, D., Weber, T., Cai, W.-J., Doney, S. C., Fennel, K., Gehlen, M., Hauck, J., Lacroix, F., Landschützer, P., Le Quéré, C., Roobaert, A., Schwinger, J., Berthet, S., Bopp, L., Chau, T. T. T., Dai, M., Gruber, N., Ilyina, T., Kock, A., Manizza, M., Lachkar, Z., Laruelle, G. G., Liao, E., Lima, I. D., Nissen, C., Rödenbeck, C., Séférian, R., Toyama, K., Tsujino, H., and Regnier, P.: A Synthesis of Global Coastal Ocean Greenhouse Gas Fluxes, *Global Biogeochemical Cycles*, 38, e2023GB007803, doi:10.1029/2023GB007803, 2024.
- Rieger, D., Bangert, M., Bischoff-Gauss, I., Förstner, J., Lundgren, K., Reinert, D., Schröter, J., Vogel, H., Zängl, G., Ruhnke, R., and Vogel, B.: ICON-ART 1.0 – a New Online-Coupled Model System from the Global to Regional Scale, *Geoscientific Model Development*, 8, 1659–1676, doi:10.5194/gmd-8-1659-2015, 2015.
- Savas, D., Dufour, G., Coman, A., Siour, G., Fortems-Cheiney, A., Broquet, G., Pison, I., Berchet, A., and Bessagnet, B.: Anthropogenic NO_x Emission Estimations over East China for 2015 and 2019 Using OMI Satellite Observations and the New Inverse Modeling System CIF-CHIMERE, *Atmosphere*, 14, 154, doi:10.3390/atmos14010154, 2023.
- Schröter, J., Rieger, D., Stassen, C., Vogel, H., Weimer, M., Werchner, S., Förstner, J., Prill, F., Reinert, D., Zängl, G., Giorgetta, M., Ruhnke, R., Vogel, B., and Braesicke, P.: ICON-ART 2.1: A Flexible Tracer Framework and Its Application for Composition Studies in Numerical Weather Forecasting and Climate Simulations, *Geoscientific Model Development*, 11, 4043–4068, doi:10.5194/gmd-11-4043-2018, 2018.
- Szénási, B., Berchet, A., Broquet, G., Segers, A., Gon, H. D. V. D., Krol, M., Hullegie, J. J. S., Kiesow, A., Günther, D., Petrescu, A. M. R., Saunois, M., Bousquet, P., and Pison, I.: A Pragmatic Protocol for Characterising Errors in Atmospheric Inversions of Methane Emissions over Europe, *Tellus B: Chemical and Physical Meteorology*, 73, 1914–1989, doi:10.1080/16000889.2021.1914989, 2021.

- Thanwerdas, J., Saunio, M., Berchet, A., Pison, I., Vaughn, B. H., Michel, S. E., and Bousquet, P.: Variational Inverse Modeling within the Community Inversion Framework v1.1 to Assimilate $\delta^{13}\text{C}(\text{CH}_4)$ and CH_4 : A Case Study with Model LMDz-SACS, *Geoscientific Model Development*, 15, 4831–4851, doi:10.5194/gmd-15-4831-2022, 2022a.
- Thanwerdas, J., Saunio, M., Pison, I., Hauglustaine, D., Berchet, A., Baier, B., Sweeney, C., and Bousquet, P.: How Do Cl Concentrations Matter for the Simulation of CH_4 and $\delta^{13}\text{C}(\text{CH}_4)$ and Estimation of the CH_4 Budget through Atmospheric Inversions?, *Atmospheric Chemistry and Physics*, 22, 15 489–15 508, doi:10.5194/acp-22-15489-2022, 2022b.
- Thanwerdas, J., Saunio, M., Berchet, A., Pison, I., and Bousquet, P.: Investigation of the Renewed Methane Growth Post-2007 with High-Resolution 3-D Variational Inverse Modeling and Isotopic Constraints, *Atmospheric Chemistry and Physics*, 24, 2129–2167, doi:10.5194/acp-24-2129-2024, 2024.
- Thanwerdas, J., Berchet, A., Constantin, L., Tsuruta, A., Steiner, M., Reum, F., Henne, S., and Brunner, D.: Improving the Ensemble Square Root Filter (EnSRF) in the Community Inversion Framework: A Case Study with ICON-ART 2024.01, *Geoscientific Model Development*, 18, 1505–1544, doi:10.5194/gmd-18-1505-2025, 2025.
- Thompson, R. L., Ishijima, K., Saikawa, E., Corazza, M., Karstens, U., Patra, P. K., Bergamaschi, P., Chevallier, F., Dlugokencky, E., Prinn, R. G., Weiss, R. F., O'Doherty, S., Fraser, P. J., Steele, L. P., Krummel, P. B., Vermeulen, A., Tohjima, Y., Jordan, A., Haszpra, L., Steinbacher, M., Van der Laan, S., Aalto, T., Meinhardt, F., Popa, M. E., Moncrieff, J., and Bousquet, P.: TransCom N₂O Model Inter-Comparison – Part 2: Atmospheric Inversion Estimates of N₂O Emissions, *Atmospheric Chemistry and Physics*, 14, 6177–6194, doi:10.5194/acp-14-6177-2014, 2014.
- Tian, H., Pan, N., Thompson, R. L., Canadell, J. G., Suntharalingam, P., Regnier, P., Davidson, E. A., Prather, M., Ciais, P., Muntean, M., Pan, S., Winiwarter, W., Zaehle, S., Zhou, F., Jackson, R. B., Bange, H. W., Berchet, S., Bian, Z., Bianchi, D., Bouwman, A. F., Buitenhuis, E. T., Dutton, G., Hu, M., Ito, A., Jain, A. K., Jeltsch-Thömmes, A., Joos, F., Kou-Giesbrecht, S., Krummel, P. B., Lan, X., Landolfi, A., Lauerwald, R., Li, Y., Lu, C., Maavara, T., Manizza, M., Millet, D. B., Mühle, J., Patra, P. K., Peters, G. P., Qin, X., Raymond, P., Resplandy, L., Rosentreter, J. A., Shi, H., Sun, Q., Tonina, D., Tubiello, F. N., van der Werf, G. R., Vuichard, N., Wang, J., Wells, K. C., Western, L. M., Wilson, C., Yang, J., Yao, Y., You, Y., and Zhu, Q.: Global Nitrous Oxide Budget (1980–2020), *Earth System Science Data*, 16, 2543–2604, doi:10.5194/essd-16-2543-2024, 2024.
- Wang, J., Vilmin, L., Mogollón, J. M., Beusen, A. H. W., van Hoek, W. J., Liu, X., Pika, P. A., Middelburg, J. J., and Bouwman, A. F.: Inland waters increasingly produce and emit nitrous oxide, *Environmental Science & Technology*, 57, 13 506–13 519, doi:10.1021/acs.est.3c02938, 2023.
- Wittig, S., Berchet, A., Pison, I., Saunio, M., Thanwerdas, J., Martinez, A., Paris, J.-D., Machida, T., Sasakawa, M., Worthy, D. E. J., Lan, X., Thompson, R. L., Sollum, E., and Arshinov, M.:

Estimating Methane Emissions in the Arctic Nations Using Surface Observations from 2008 to 2019, *Atmospheric Chemistry and Physics*, 23, 6457–6485, doi:10.5194/acp-23-6457-2023, 2023.

World Meteorological Organization: Scientific Assessment of Ozone Depletion: 2022, Tech. Rep. GAW Report No. 278, World Meteorological Organization, URL <https://www.cs1.noaa.gov/assessments/ozone/2022>, last access: 26 February 2023, 2022.

Zängl, G., Reinert, D., Rípodas, P., and Baldauf, M.: The ICON (ICOsahedral Non-hydrostatic) Modelling Framework of DWD and MPI-M: Description of the Non-Hydrostatic Dynamical Core, *Quarterly Journal of the Royal Meteorological Society*, 141, 563–579, doi:10.1002/qj.2378, 2015.